Theory of multiwall carbon nanotubes as waveguides and antennas in the infrared and the visible regimes

M. V. Shuba, G. Ya. Slepyan, and S. A. Maksimenko
Institute for Nuclear Problems, Belarus State University, Bobruiskaya 11, 220050 Minsk, Belarus

C. Thomsen
Institut für Festkörperphusik, Technische Universität Berlin, Hardenbergstr. 36, D-10623 Berlin, Germany

A. Lakhtakia
Department of Engineering Science and Mechanics, Nanoengineered Metamaterials Group, Pennsylvania State University, University Park, Pennsylvania 16802-6812, USA

(Received 12 June 2008; revised manuscript received 18 January 2009; published 1 April 2009)

The propagation of azimuthally symmetric guided waves in multiwalled carbon nanotubes (MWCNTs) was analyzed theoretically in the midinfrared and the visible regimes. The MWCNTs were modeled as ensembles of concentric, cylindrical, conducting shells. The influence of intershell electron tunneling on the optical properties of MWCNTs was examined by focusing on a double-walled carbon nanotube (DWCNT). Longitudinal electrostatic waves exist in DWCNTs due to intershell tunneling. Conditions for weak influence of intershell tunneling in DWCNTs were identified, and an integral-equation approach for scattering by an MWCNT was formulated when those conditions prevail. Slightly attenuated guided waves and antenna resonances due to the edge effect exist for not-too-thick MWCNTs in the far-infrared and the midinfrared regimes. Interband transitions retard the propagation of guided waves and have a deleterious effect on the performance of a finite-length MWCNT as a nanoantenna. Propagation of surface-plasmon waves along an MWCNT with a gold core was also analyzed. In the near-infrared and the visible regimes, the shells behave effectively as lossy dielectrics to suppress surface-plasmon-wave propagation along the gold core.

DOI: 10.1103/PhysRevB.79.155403 PACS number(s): 42.70.−a, 73.25.+i, 77.84.Lf, 78.67.Ch

I. INTRODUCTION

Their unusual physical and chemical properties and their potential applications in a variety of nanotechnologies make carbon nanotubes (CNTs) very interesting objects to technoscientists[1,2] despite possible health hazards.[3] In particular, CNTs have been proposed to fabricate several different integrated-circuit elements and electromagnetic devices, such as transmission lines,[4–8] interconnects,[9–12] and nanoantennas.[13–20] The fabrications of a CNT-based amplitude modulator/demodulator[21] and a fully integrated radio receiver[22] have been reported. References 23–29 demonstrate the potential of CNTs as emitters of terahertz and infrared radiation.

Not surprisingly, the electromagnetic characteristics of CNT-based antennas have been examined in different frequency regimes ranging from the microwave to the visible. CNT morphology has been demonstrated to play a crucial role, as evinced by reported research on single-walled carbon nanotubes (SWCNTs),[14–16,30] ~1-cm-long one-dimensional (1D) chains of electrically connected SWCNTs,[15] planar periodic structures of SWCNTs,[31,32] CNT bundles,[33,34] and CNT arrays.[35] Continuing in that vein, here we report our work on the performance of multiwalled carbon nanotubes (MWCNTs) as antennas.

A multiwalled CNT comprises N concentric shells (or tubes), each obtained by rolling a graphene sheet into a cylinder. The number of shells in an MWCNT can range from 2 to 200, and the distance between consecutive shells from 3.4 to 3.6 Å,[36] which is close to the interlayer distance in graphite (3.35 Å). The lattice structures of consecutive shells are generally uncorrelated with each other and can even have different chiralities. In fact, several experiments on MWCNTs have indicated that often the different shells have different periodicities.[37,38] Two consecutive shells of an MWCNT are called commensurate (incommensurate) if the ratio of their unit-cell lengths along the CNT axis is rational (irrational), indicating the presence (absence) of translational symmetry. Incommensurability affects the transport and optical properties of MWCNTs.[39–46]

The critical issue when modeling the electromagnetic properties of an MWCNT is the intershell interaction leading to intershell electron tunneling or hopping. Published data, although very variable, show a strong dependence on the intrinsic symmetries of the shells, which dictates selection rules for the elements of the tunneling matrix, as determined by the conservation laws for energy and momentum. As may be expected, two incommensurate shells interact differently than two commensurate cells.[39–46] For example, the Fermi momenta of two incommensurate shells do not coincide within the first Brillouin zone and therefore the intershell tunneling vanishes.[43]

An isolated MWCNT can be modeled in several different ways. Abrikosov *et al.*[47] considered an MWCNT as a set of coaxial, continuous, conducting cylinders accompanied by an appropriate Kronig-Penney-type potential in the radial direction. Dyachkov and Makaev[48] as well as Tunney and Cooper[49] assumed the intershell interaction to be so small that each shell could be considered to be in a perturbed eigenstate of an SWCNT. A computer simulation with some

input parameters extracted from experiment has also been reported.[50]

Following Refs. 48 and 49, although the intershell interaction in defectless double-walled carbon nanotubes (DWCNT) shifts optical band gaps and distorts the density of electronic states, it does not subvert the intrinsic type of conductivity (either metallic or semiconductor).[47–50] The impact of weak intershell interaction (i.e., tunneling) on the optical properties of an MWCNT should not be assumed *ab initio* to be weak, as we found out that intershell tunneling leads to new branches in MWCNT spectra.

Analysis of the physical characteristics of CNT-based integrated circuit elements, such as antennas, must follow the general principles of electrodynamics and must account for the peculiar dispersion properties of electrons in CNTs. A key element of the analysis is the formulation of the effective boundary conditions (EBCs) for the electromagnetic field on the CNT surface.[4–6] In this paper, we incorporate the presence of intershell tunneling in the EBCs, showing thereby that tunneling alters the EBCs significantly from the EBCs presented in Refs. 4–6.

In order to incorporate intershell tunneling in the EBCs, we adopt a microscopic approach. The application of this approach and the role of intershell tunneling is exemplified in Sec. II for a DWCNT ($N=2$). The conditions leading to weak influence of intershell tunneling are also identified in that section. Since the radiation characteristics of an MWCNT are determined by its waveguiding properties, the dispersion equation for azimuthally symmetric guided-wave propagation on an infinitely long DWCNT is derived in Sec. II B. Assuming that the conditions for the influence of intershell tunneling being weak enough to be ignored are valid, we formulate a numerical solution of the boundary-value problem for scattering by a finite-length MWCNT by exploiting an integral-equation technique in Sec. III. Our approach is well established in antenna theory[51] and has been successfully applied to SWCNT antennas[14] and almost circular bundles of closely packed SWCNTs.[33] Section IV contains numerical results for guided-wave parameters (slow wave and attenuation) and the scattering properties of MWCNT in a wide frequency range from the terahertz to the visible regimes. Section V presents an assessment of the potential of an isolated MWCNT function as an optical nanoantenna. Concluding remarks are provided in Sec. VI. An $\exp(-i\omega t)$ time dependence is implicit, t denotes the time, $\omega=2\pi f$ is the angular frequency, and f is the frequency. The position vector $\mathbf{r}$ is represented in a cylindrical coordinate system (ρ,ϕ,z) with $\mathbf{e}_\rho$, $\mathbf{e}_\phi$, and $\mathbf{e}_z$ as the unit vectors. All fields are assumed to be independent of ϕ.

II. ELECTRODYNAMICS OF A DWCNT: INTERSHELL TUNNELING

Our aim in this section is to incorporate intershell tunneling in CNT electrodynamics. For simplicity, we consider intershell tunneling in a DWCNT, the generalization for an MWCNT with three and more shells thereafter being simple.

Let the chosen DWCNT consist of two infinitely long, conducting, coaxial cylindrical shells with cross-sectional radii R_2 and R_1 $(R_2>R_1)$. Both shells are assumed to be conducting, the low-frequency conductivity being caused mainly by electrons with energy near the Fermi level.

Our task is to calculate the axial surface current density in each shell when the DWCNT is illuminated by a time-harmonic electromagnetic field. Electron transport on each shell can be described by the tight-binding approximation, taking into account the transverse quantization of the motion of charge carriers and the hexagonal structure of the graphene lattice.[1] The influence of the Coulomb interaction on the charge-carrier motion is neglected.

A. Effective boundary conditions

Let the cylindrical axis of the chosen DWCNT be aligned parallel to the z axis and the centroid of the DWCNT be located at the origin of the coordinate system. Let $|\alpha_p\rangle$, $p\in\{1,2\}$, be the one-electron wave function of the pth shell. This wave function is characterized by three variables; i.e., $|\alpha_p\rangle\equiv\{\tilde{\lambda},p_z,s\}_p$, where $\tilde{\lambda}$ is an index corresponding to the conductance or valence bands, p_z is the axial projection of the quasimomentum of an electron, and the integer s characterizes the transverse quasimomentum of a π electron. The main properties of $|\alpha_p\rangle$ are presented in Appendix A.

Let the two shells be coupled through the electron tunneling, such that only intraband tunnel transitions of π electrons with identical momentum are permitted. Then the Hamiltonian of the isolated DWCNT is $\hat{\mathcal{H}}_0+\Delta\hat{\mathcal{H}}$, where

$$\hat{\mathcal{H}}_0=\sum_\alpha \mathcal{E}_\alpha^{(1)}|\alpha_1\rangle\langle\alpha_1|+\mathcal{E}_\alpha^{(2)}|\alpha_2\rangle\langle\alpha_2| \tag{1}$$

and

$$\Delta\hat{\mathcal{H}}=\hbar\omega_t\sum_\alpha\left(|\alpha_1\rangle\langle\alpha_2|+|\alpha_2\rangle\langle\alpha_1|\right). \tag{2}$$

Here, $\hat{\mathcal{H}}_0$ corresponds to electron motion in the absence of intershell tunneling and $\mathcal{E}_\alpha^{(p)}$ is the one-electron energy associated with $|\alpha_p\rangle$. Let us assume that $\mathcal{E}_\alpha^{(1)}\cong\mathcal{E}_\alpha^{(2)}=\mathcal{E}_\alpha=N_{\tilde{\lambda}}^-\mathcal{E}(p_z,s)$, where $N_{\tilde{\lambda}}^-=1$ for the conduction band and $N_{\tilde{\lambda}}^-=-1$ for the valence band. This assumption can be justified in the low-frequency regime by virtue of an electron dispersion law such as Dirac's law in the vicinity of the Fermi energy $\mathcal{E}(p_z,s)\cong v_F|p_z|$, which is identical for all metallic shells, v_F being the π-electron speed at the Fermi level. The component $\Delta\hat{\mathcal{H}}$ of the Hamiltonian describes electron tunneling between the shells. The quantity ω_t is the angular frequency of tunneling, which we assume is the same for all $|\alpha_p\rangle$, and $\hbar$ is the reduced Planck constant. The interaction of the DWCNT with the incident electromagnetic field can be described by the Hamiltonian $\hat{\mathcal{H}}_I=e\mathcal{V}\hat{I}$, where e is the electronic charge, $\mathcal{V}$ is the spatiotemporally varying, azimuthally symmetric electric potential, and $\hat{I}$ is the identity matrix.

Suppose that the electromagnetic field depends on z as $\exp(ihz)$, where h would be identified later as a guide wave number. Let us calculate the surface charge density $n_{Sp}(h,\omega)$ induced by the electromagnetic field on the pth shell. The electric field intensity is supposed to be low and Hamiltonian

$\hat{\mathcal{H}}_I$ is considered as a small perturbation for the motion of the charge carriers. Omitting intermediate steps provided in Appendix A, we present here the final result for the first $(p=1)$ shell,

$$n_{S1}(h,\omega) = \frac{e}{4\pi^2\hbar R_1}[(V_1+V_2)\varphi_+(h,\omega) + (V_1-V_2)\varphi_-(h,\omega)], \tag{3}$$

where V_p is the Fourier amplitude of the electric potential on the surface of pth shell, along with

$$\varphi_\pm(h,\omega) = \sum_s \int_{1\text{stBz}} dp_Z \sum_{\tilde{\lambda}\tilde{\lambda}'} |M_{\alpha\alpha'}|^2 A^{\pm}_{\alpha\alpha'}, \tag{4}$$

$$A^{+}_{\alpha\alpha'} = \frac{F(\mathcal{E}_{\alpha'} + N^{\tilde{\lambda}}_{\tilde{\lambda}'}\hbar\omega_t) - F(\mathcal{E}_\alpha + N^{\tilde{\lambda}}_{\tilde{\lambda}}\hbar\omega_t)}{\mathcal{E}_{\alpha'} - \mathcal{E}_\alpha + (N^{\tilde{\lambda}}_{\tilde{\lambda}'} - N^{\tilde{\lambda}}_{\tilde{\lambda}})\hbar\omega_t - \hbar\omega - i0} + \frac{F(\mathcal{E}_{\alpha'} - N^{\tilde{\lambda}}_{\tilde{\lambda}'}\hbar\omega_t) - F(\mathcal{E}_\alpha - N^{\tilde{\lambda}}_{\tilde{\lambda}}\hbar\omega_t)}{\mathcal{E}_{\alpha'} - \mathcal{E}_\alpha - (N^{\tilde{\lambda}}_{\tilde{\lambda}'} - N^{\tilde{\lambda}}_{\tilde{\lambda}})\hbar\omega_t - \hbar\omega - i0}, \tag{5}$$

$$A^{-}_{\alpha\alpha'} = \frac{F(\mathcal{E}_{\alpha'} + N^{\tilde{\lambda}}_{\tilde{\lambda}'}\hbar\omega_t) - F(\mathcal{E}_\alpha - N^{\tilde{\lambda}}_{\tilde{\lambda}}\hbar\omega_t)}{\mathcal{E}_{\alpha'} - \mathcal{E}_\alpha + (N^{\tilde{\lambda}}_{\tilde{\lambda}'} + N^{\tilde{\lambda}}_{\tilde{\lambda}})\hbar\omega_t - \hbar\omega - i0} + \frac{F(\mathcal{E}_{\alpha'} - N^{\tilde{\lambda}}_{\tilde{\lambda}'}\hbar\omega_t) - F(\mathcal{E}_\alpha + N^{\tilde{\lambda}}_{\tilde{\lambda}}\hbar\omega_t)}{\mathcal{E}_{\alpha'} - \mathcal{E}_\alpha - (N^{\tilde{\lambda}}_{\tilde{\lambda}'} + N^{\tilde{\lambda}}_{\tilde{\lambda}})\hbar\omega_t - \hbar\omega - i0}. \tag{6}$$

Other quantities appearing in Eqs. (4)–(6) are provided in Appendix A.

The surface charge density $n_{S2}(h,\omega)$ can be found from Eq. (3) after implementing the replacement $\{R_1 \to R_2,\ V_{1,2} \to V_{2,1}\}$ therein. Let the vectors $\mathbf{E}$ and $\mathbf{H}$ denote the electric and the magnetic fields, respectively. The z-directed components of the surface current density and the electric field on the pth shell can be found from Eq. (3) as $J_{zp}(h,\omega) = e\omega n_{Sp}(h,\omega)$ and $E_{zp} = -ihV_p$, $p \in \{1,2\}$, respectively. Then we have

$$J_{z1} = \sigma_{11}(h,\omega)E_{z1} + \sigma_{12}(h,\omega)E_{z2},$$

$$J_{z2} = \sigma_{21}(h,\omega)E_{z1} + \sigma_{22}(h,\omega)E_{z2}. \tag{7}$$

Here,

$$J_{zp} = \frac{c}{4\pi}(H_\phi|_{R_p+0} - H_\phi|_{R_p-0}), \tag{8}$$

where c is the speed of light in free space (i.e., vacuum),

$$\sigma_{11}(h,\omega) = -\frac{ie^2\omega}{4\pi^2\hbar R_1 h^2}[\varphi_+(h,\omega) + \varphi_-(h,\omega)], \tag{9}$$

$$\sigma_{12}(h,\omega) = -\frac{ie^2\omega}{4\pi^2\hbar R_1 h^2}[\varphi_+(h,\omega) - \varphi_-(h,\omega)], \tag{10}$$

and the quantities $\sigma_{22}(h,\omega)$ and $\sigma_{21}(h,\omega)$ follow from Eqs. (9) and (10), respectively, after implementing the replacement $R_1 \to R_2$.

Equations (7) and (8) constitute a generalization of the EBCs derived originally for SWCNTs.[4] The boundary condition for E_z to be continuous across the surface of each shell remains identical to the case of SWCNT. The matrix $\hat{\sigma}(h,\omega)$ with elements $\sigma_{pq}(h,\omega)$ can be considered as a generalized susceptibility of the DWCNT. Whereas $\sigma_{11}(h,\omega)$ and $\sigma_{22}(h,\omega)$ can be interpreted as the intrinsic conductivities of the shells, $\sigma_{12}(h,\omega)$ and $\sigma_{21}(h,\omega)$ can be considered as the mutual surface conductivities. The existence of the mutual surface conductivities implies the *transverse nonlocal response* of a DWCNT: the spatial dispersion in the radial direction.

The integral over p_z in Eq. (4) must be calculated as a principal-value integral; i.e.,

$$\frac{1}{\Phi(p_z) - i0} = \mathcal{P}\frac{1}{\Phi(p_z)} + i\pi\frac{\delta(p_z - p_{z0})}{\Phi'(p_{z0})}, \tag{11}$$

where p_{z0} is the root of the equation $\Phi(p_z)=0$, the prime indicates the derivative with respect to the argument, $\mathcal{P}$ indicates the principal value, and $\delta(x)$ is the Dirac delta function. As follows from Eq. (11), $\sigma_{pq}(h,\omega)$ is generally a complex-valued quantity. The first term on the right side of Eq. (11) corresponds to nonrelaxation part of the conductivity, while the second term corresponds to the collisionless relaxation (Landau damping). Let us note that both intrinsic and mutual conductivities contribute to the collisionless relaxation in a DWCNT. The collision relaxation in the τ approximation can be taken into account by means of the standard replacement $(\omega+i0)^2 = \omega(\omega+i\tau^{-1})$, where τ is the relaxation time. Eigenwaves can be initially analyzed in the absence of relaxation, whose effect can later be considered as a small perturbation.

In the limit $\omega_t \to 0$ we have $\sigma_{12,21}(h,\omega) \to 0$ and $\sigma_{pp}(h,\omega) \to \sigma_p$, where σ_p is the axial conductivity of the isolated pth shell provided in Ref. 5. In the same limit, the EBCs [Eq. (7)] transform to EBCs for an MWCNT comprising noninteracting shells,[4] where each shell acts as an SWCNT with identical parameters. Applying the Hertz vector representation, as shown in Appendix B, and using Eqs. (B2) and (B3), we can obtain the EBCs across the pth shell of the MWCNT as

$$\left.\frac{\partial\Pi}{\partial\rho}\right|_{\rho=R_p+0} - \left.\frac{\partial\Pi}{\partial\rho}\right|_{\rho=R_p-0} = \frac{4\pi}{ikc}J_p, \tag{12}$$

$$\Pi|_{\rho=R_p+0} = \Pi|_{\rho=R_p-0}. \tag{13}$$

Here $\mathbf{J}_p(z) = J_p(z)\mathbf{e}_z$ is the axial current density on the surface $\rho=R_p$, with

$$J_p(z) = \sigma_p\left(\frac{d^2}{dz^2} + k^2\right)\Pi(R_p,z). \tag{14}$$

Clearly, this model has restricted applicability because intershell interaction has been ignored therein.

In the low-frequency regime ($\hbar\omega \le 0.1$ eV) we can neglect the influence of optical transitions between the valence and conduction bands. As a result, in Eq. (4) we can retain only the terms with $\tilde{\lambda} = \tilde{\lambda}'$ and set $|M_{\alpha\alpha'}|^2 \approx 1$.[5] Then the electromagnetic response characteristics of the chosen DWCNT are only due to intraband transitions of π electrons

[Eq. (5)] and quantum transitions between subbands with different indices ζ discussed in Appendix A [Eq. (6)]. The transitions of the first type yield a Drude term with small corrections caused by intershell tunneling, and the transitions of the second type lead to resonance at the frequency $\omega \cong 2\omega_t$.

The resonance is caused entirely by intershell tunneling. As is shown in the remainder of this section, tunneling leads to qualitatively different effects not only in the vicinity of the tunneling resonance. The reason is the strong *longitudinal nonlocality*: a strong dependence on h. Indeed, $\lim_{h\to 0} \varphi_+(h,\omega)=O(h^2)$, while $\lim_{h\to 0} \varphi_-(h,\omega)=O(1)$. This implies that longitudinal spatial dispersion slightly corrects the Drude term but entirely determines the contribution of tunneling transitions to the DWCNT response. This contribution corresponds to the term $O(h^{-2})$ in the generalized susceptibility.

The frequency-domain Maxwell equations with EBCs [Eq. (7)] are suitable for describing the electromagnetic field inside ($\rho \le R_1$) and outside ($\rho \ge R_2$) the DWCNT, but do not for describing the field between the two shells ($R_1 < \rho < R_2$). Such a situation is not unexpected and indeed is characteristic of the EBC technique.[52] This situation arises due to the existence of an intershell current, which should be included in the Maxwell equations. In the EBC technique, the intershell current is removed from the Maxwell equations, but its contribution into the field formation is taking into account by the corresponding terms in Eq. (7).

B. Dispersion characteristics of azimuthally symmetric guided waves in the DWCNT

Let us find the solution of the Maxwell equations for the chosen DWCNT in the form of an azimuthally symmetric traveling wave $\exp[i(hz-\omega t)]$ satisfying the EBCs [Eq. (7)], the continuity of E_z across the surfaces of both shells, and the condition of exponential attenuation as $\rho \to \infty$. The Hertz potential of this wave is

$$\Pi(\rho,z) = e^{ihz}\sum_{p=1}^{2} A_p \Phi_p(\rho), \tag{15}$$

where h can now be identified as the unknown guide wave number, the basis functions $\Phi_p(\rho)$ are presented in Appendix B, and $\{A_p\}$ is the set of unknown coefficients. The continuity condition of E_z and condition of attenuation as $\rho \to \infty$ are automatically satisfied due to the properties of the functions $\Phi_p(\rho)$.

The use of Eq. (15) in Eqs. (7), (8), (B2), and (B3) leads to a system of linear homogeneous equations with respect to the coefficients A_p. A nontrivial solution of the system is provided by the dispersion equation

$$\det(\hat{\sigma}\cdot\hat{M}-\hat{B}) = 0, \tag{16}$$

where the element $\sigma_{pq}(h,\omega)$ of the matrix $\hat{\sigma}$ is provided in Sec. II A, the element M_{pq} of the matrix $\hat{M}$ is

$$M_{pq} = \begin{cases} K_0(\kappa R_q) I_0(\kappa R_p), & q \ge p \\ K_0(\kappa R_p) I_0(\kappa R_q), & q < p, \end{cases} \tag{17}$$

and the element B_{pq} of the diagonal matrix $\hat{B}$ is

$$B_{pq} = i\omega\delta_{pq}/(4\pi R_q \kappa^2). \tag{18}$$

In the foregoing equations, $\kappa=\sqrt{h^2-k^2}$, $k=\omega/c$ is the free-space wave number, δ_{qp} is the Kronecker delta, and $I_0(\cdot)$ and $K_0(\cdot)$ are modified Bessel functions. The transcendental Eq. (16) yields the values of $h \equiv h(\omega)$.

Let us note that the formulation for guided waves in an MWCNT with an arbitrary number of shells can also be described by the foregoing method: the summation over p in Eq. (15) is then from 1 to N, whereas $\hat{\sigma}$, $\hat{M}$, and $\hat{B}$ are $N \times N$ matrixes. The forms of Eq. (16) and the matrix elements M_{pq} and B_{pq} do not change. Only those nondiagonal elements of the matrix $\hat{\sigma}$ are not equal to zero, which correspond to shells coupled by tunneling.

For obtaining the dispersion characteristics using Eq. (16), the angular frequency of tunneling ω_t must be known *a priori*. Thus, ω_t is a phenomenological parameter in our formulation. Even for defectless DWCNTs, ω_t depends on different factors and can vary in a wide range. The theoretical estimation of ω_t is by itself a sufficiently complicated task, the results being highly dependent on the assumptions.[50] For all numerical results reported in this paper, we extracted ω_t from experimental data. Assuming elastic tunneling and applying the Landauer-Butikker equation,[53] one can obtain the tunneling conductance G_{atom} through the π orbital between two atoms in different shells as

$$G_{\text{atom}} \simeq \frac{8\pi e^2}{\hbar R_1 R_2}\left(\frac{S\omega_t}{v_F}\right)^2, \tag{19}$$

where $S=2.6$ Å^2 is the area of the surface occupied by one atom. Comparing Eq. (19) with data from Ref. 50, we get $\hbar\omega_t \le 35$ meV, in agreement with reported values for graphite[50] and a DWCNT with (5,5) and (10,10) shells.[46] Accordingly, we used the value $\omega_t = 10^{13}$ rad s^{-1} for the calculations reported in Sec. II. Parenthetically, Eq. (19) through the value of ω_t determines the relation between the static tunneling conductance of the DWCNT and its dynamic conductivity matrix $\hat{\sigma}$ defined via Eqs. (9) and (10).

The number of surface guided-wave modes is equal to the number of shells N. Figure 1 exemplifies the dispersion characteristics of the two guided-wave modes in a DWCNT. Modes with in-phase or antiphase currents on the shells exist, which property determines the shape of a modal dispersion curve. Strictly speaking, because of the cylindrical geometry the considered modes have no symmetry with respect to ρ in the region $R_1 \le \rho \le R_2$ about the cylindrical surface $\rho=(R_1+R_2)/2$. Each mode is a superposition of symmetric and asymmetric field components, but for each mode only one of the components is dominant. Therefore, we refer to these modes as *symmetriclike* and *asymmetriclike* modes.

Figure 1 shows that the asymmetriclike mode is more retarded than the symmetriclike mode. For both modes, the retardation sufficiently decreases in the range of $\omega \cong 2\omega_t$. For comparison, the dispersion curves are also shown when in-

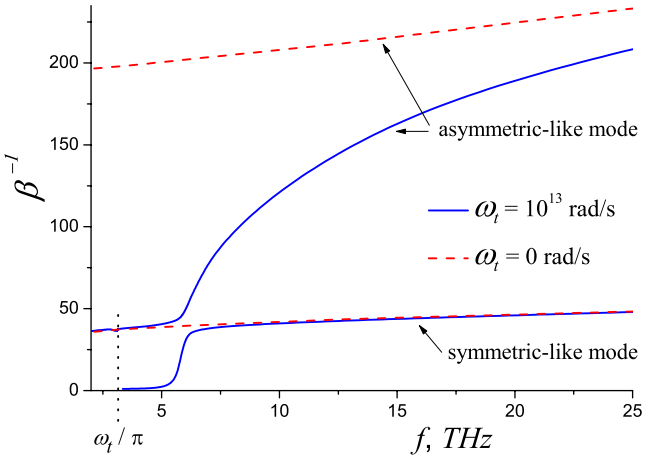

FIG. 1. (Color online) Frequency dependence of the inverse slow-wave coefficient $\beta^{-1}=h/k$ for guided-wave modes in a DWCNT with (9,0) and (18,0) shells; $\omega_t=10^{13}$ rad s^{-1}. The solid lines show results with intershell tunneling; the dashed lines without.

tershell tunneling is ignored ($\omega_t=0$) by setting $\sigma_{pq}=\delta_{pq}\sigma_p$.[4] Clearly, intershell tunneling very slightly affects the symmetriclike mode, except in the immediate vicinity of tunneling resonance $\omega\cong 2\omega_t$. In contrast, intershell tunneling strongly affects the asymmetriclike mode over a wide frequency range. Thus, intershell tunneling can be ignored only in specific circumstances.

C. Longitudinal electrostatic modes in the DWCNT

Let us next seek solutions in the electrostatic approximation[54,55] by setting $\mathbf{H}=\mathbf{0}$ everywhere. Then, $\nabla\times\mathbf{E}=\mathbf{0}$ and $\nabla\cdot\mathbf{E}=0$, which can be satisfied if $\mathbf{E}=-\nabla V$. The temporally constant scalar potential $V(\rho,z)$ is a solution of the Laplace equation,

$$\nabla^2 V = 0. \tag{20}$$

According to Eq. (8), $J_{z1}=J_{z2}=0$, so that Eq. (7) becomes

$$\sigma_{11}(h,\omega)E_{z1} + \sigma_{12}(h,\omega)E_{z2} = 0,$$

$$\sigma_{21}(h,\omega)E_{z1} + \sigma_{22}(h,\omega)E_{z2} = 0. \tag{21}$$

A nontrivial solution exists if $\sigma_{11}(h,\omega)\sigma_{22}(h,\omega)=\sigma_{12}(h,\omega)\sigma_{21}(h,\omega)$, which amounts to

$$\varphi_-(h,\omega) = 0. \tag{22}$$

Let us note that last equation does not include the cross-sectional dimensions of the CNT shells. The solution of Eq. (22) depends on the type of CNT shells through the angular frequency of tunneling ω_t. There are two positive real roots of Eq. (22) at a given value of $\omega<2\omega_t$, while there is only one root when $\omega>2\omega_t$, as shown in Fig. 2. One of the two roots in the range $\omega<2\omega_t$ indicates *anomalous dispersion*. Each of these roots corresponds to the guided-wave traveling along the $+z$ direction. As Eq. (22) is invariant with respect to the replacement $h\to -h$, wave propagation along the $-z$ direction occurs analogously. As $\omega\to\infty$ the asymptotic solution of Eq. (22) has the form $h=\pm\omega/v_F$. Of cause, the region of this asymptotic solution is limited by the appearance of optical transitions.

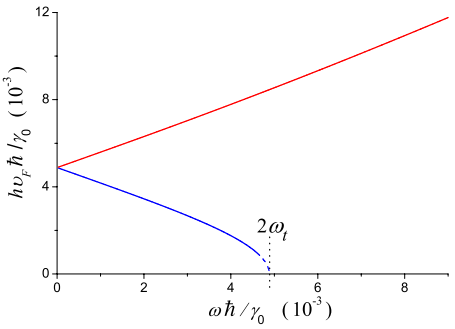

FIG. 2. (Color online) Frequency dependence of the guide wave number h in the electrostatic approximation. $\gamma_0\approx 2.7$ eV is the overlap integral (Ref. 1) (see Fig. 1 for other details).

The vicinity of tunnel resonance $\omega\cong 2\omega_t$ for one of the branches is marked by the dashed line in Fig. 2. In that vicinity, the applicability condition of electrostatic approximation ($h\gg k$) breaks down for this branch and a more rigorous analysis is required. At $\omega=0$ both branches intersect at a finite value of h. Thus, intershell tunneling qualitatively changes the character of Coulomb screening in a DWCNT: the Coulomb potential of a point charge, placed at the center of the DWCNT, varies as $\cos(hz)$. This effect is analogous to the Kohn anomaly in metals and degenerate plasmas,[56] but the singularity is stronger (pole). The reason is the low-dimensional nature of charge motion in DWCNT.

The longitudinal modes arise due to intershell tunneling and therefore have no analog in SWCNTs. These modes to a certain extent are similar to the longitudinal waves in degenerate plasmas[56] and in crystals with spatial dispersion.[55]

From Eq. (21), $E_{z1}=-E_{z2}$ if Eq. (22) is satisfied. In other words, a longitudinal mode always has antiphase properties: the z component of the electric field is oppositely directed on the surfaces of the two shells. To calculate the electric field distribution, one needs to solve Eq. (20) in the form of the traveling wave, which has antiphase properties, satisfies the regularity condition at $\rho=0$, and asymptotically varies as $\log(\rho)$ as $\rho\to\infty$. Then, the relation

$$V(\rho,z,t) = Ae^{i(hz-\omega t)}\begin{cases} I_0(h\rho), & 0<\rho<R_1 \\ \dfrac{-I_0(hR_1)}{K_0(hR_2)}K_0(h\rho), & \rho>R_2, \end{cases} \tag{23}$$

where A is an arbitrary constant, whereas h and ω are related by Eq. (22).

III. LIGHT SCATTERING BY A FINITE-LENGTH MWCNT

Moving on to MWCNTs, let us model an MWCNT as a multishell structure comprising N coaxial infinitesimally thin cylinders in free space. Let us enumerate the shells in the MWCNT consecutively from 1 to N beginning from the innermost shell, so that their cross-sectional radii comply with

the condition $R_N > R_{N-1} > \cdots > R_1$. The cross-sectional radius R_N of the outermost shell is assumed to be much smaller than the free-space wavelength $\lambda = 2\pi/k$. The transverse current density in every shell is neglected.

The model of an MWCNT as an assembly of isolated, coaxially rolled, graphene sheets was introduced by Longe and Bose.[57] This model is often used to study plasmon modes in MWCNTs.[58–62] It has also been used for MWCNT interconnects,[63] MWCNT antennas,[19] and MWCNT inductors.[64] In order to study guided waves in a finite-length MWCNT, we improved this simple model by taking into account the edge effects at both ends of the MWCNT—which step allowed us to systematically describe the antenna effect in MWCNTs of different sizes in different frequency regimes.

Most MWCNTs of large outer cross-sectional diameter (50–300 nm) do not possess a coaxially layered morphology and also contain a lot of defects. Nevertheless, very pure and coaxially layered MWCNTs with outer diameter of 100 nm have been fabricated by Li *et al.*[65] These MWCNTs have a large current-carrying capacity. The extremely high conductivity was explained by Li *et al.*[65] on the basis of the MWCNT being made of coaxial layers, each with the same band structure as an SWCNT.

Intershell tunneling in MWCNTs is neglected in the remainder of this paper. Such an approximation can be justified (i) for symmetriclike modes with approximately identical current distribution in adjacent shells and (ii) at frequencies which are much higher than the tunneling frequency. These two conditions limit the applicability of results presented in Secs. III A and IV. Having made the approximation, we can take the conductivity σ_p of pth shell, $p \in [1,N]$, to be the same as for an SWCNT with identical geometrical parameters; an explicit expression for σ_p can be found in Ref. 4.

A. Integral-equation technique

Let us now consider the scattering of an electromagnetic wave incident on an MWCNT of finite length L. The incident field is assumed to be spatially homogenous in the MWCNT cross section. Therefore, it couples only slightly with those guided waves that have antiphase current in adjacent shells. As shown in Sec. II B, outside the narrow vicinity of a tunneling resonance, intershell tunneling strongly affects only such guided waves. Therefore, *exclusion of intershell* tunneling means that we must exclude this narrow frequency regime from consideration.

The scattered field can be described by Eqs. (B2) and (B3) with the electric Hertz potential satisfying the Helmholz equation [Eq. (B1)], the usual radiation condition,[51] and the boundary conditions (12) and (13). The surface current density $J_p(z)$ at $\rho = R_p$, $p \in [1,N]$, is given by

$$J_p(z) = \sigma_p \left(\frac{d^2}{dz^2} + k^2 \right) \Pi(R_p, z) + \sigma_p E_z^{(0)}(R_p, z), \tag{24}$$

where $E_z^{(0)}(\rho, z)$ is the z component of the incident electric field. As the intershell tunneling through the two ends of the MWCNT is negligible, the current density $J_p(z)$ satisfies the edge conditions,

$$J_p(\pm L/2) = 0, \tag{25}$$

thereby expressing the absence of concentrated charges on the ends. The boundary-value problem can effectively be solved by the integral-equation technique for the surface current density as follows.[54,66]

The potential $\Pi(\rho, z)$ must be linearly related to $J_p(z)$, $p \in [1,N]$, as

$$\Pi(\rho, z) = \frac{i}{\omega} \sum_{p=1}^{N} R_p \int_{-L/2}^{L/2} J_p(z') G(z - z', \rho, R_p) dz', \tag{26}$$

where

$$G(z, \rho, R) = \int_0^{2\pi} \frac{\exp(ik\sqrt{\rho^2 + R^2 - 2R\rho \cos \phi + z^2})}{\sqrt{\rho^2 + R^2 - 2R\rho \cos \phi + z^2}} d\phi \tag{27}$$

is the free-space Green's function for Eq. (B1). Setting $\rho = R_q$ in Eq. (26) and making use of Eq. (24), we arrive at the following system of N integral equations with respect to unknown current densities:

$$-\frac{1}{2ik} \int_{-L/2}^{L/2} E_z^{(0)}(R_q, z) \exp(ik|z - z'|) dz' + C_q \exp(ikz) + D_q \exp(-ikz) = \sum_{p=1}^{N} \int_{-L/2}^{L/2} \left[\frac{2\pi i R_p}{\omega} G(z - z', R_p, R_q) + \frac{i\delta_{qp}}{2k\sigma_p} \exp(ik|z - z'|) \right] J_p(z') dz', \quad q \in [1,N]. \tag{28}$$

Here, C_q and D_q, $q \in [1,N]$, are unknown constants to be determined from the edge conditions [Eq. (25)].

In the long-wavelength regime ($\lambda \gg L$), the electromagnetic scattering properties of the MWCNT can be encapsulated in a polarizability tensor with only one nonzero component,

$$\alpha_{zz} = \frac{2\pi i}{\omega E_z^{(0)}(0,0)} \sum_{p=1}^{N} R_p \int_{-L/2}^{L/2} J_p(z) dz. \tag{29}$$

The integral on the right side of Eq. (28) can be numerically handled by a quadrature formula that leads to a finite system of linear algebraic equations.[67] The numerical inversion of the matrix of the system obtained gives the approximate solution of integral Eq. (28). Parenthetically, the foregoing formalism was recently applied to almost circular closely packed bundles of finite-length parallel, identical, metallic SWCNTs.[33]

A finite-length MWCNT functioning as a receiving antenna can be characterized by the antenna efficiency,[33]

$$\eta = \frac{P_r}{P_t + P_r}, \tag{30}$$

where

$$P_r = \frac{\pi^2 k^2}{c} \int_0^{\pi} \sin^3\theta \left| \int_{-L/2}^{L/2} e^{ikz\cos\theta} \sum_{p=1}^{N} R_p J_p(z) dz \right|^2 d\theta \tag{31}$$

is the scattered power,

$$P_t = \pi \sum_{p=1}^{N} R_p \, \mathrm{Re}\left(\frac{1}{\sigma_p}\right) \int_{-L/2}^{L/2} |J_p(z)|^2 dz \tag{32}$$

is the power lost to Ohmic dissipation, and θ is an angle with respect to the z axis.

B. Interband-transition regime: Born approximation

According to Refs. 16 and 32, surface waves in a CNT are strongly attenuated in the frequency regime of interband transitions. Therefore, the surface current density $J(z)$ in an SWCNT of radius R exposed to an incident electric field $\mathbf{E}^{(0)}$ obeys Ohm's law,

$$J(z) = \sigma E_z^{(0)}(R,z), \tag{33}$$

very well, the scalar σ being the surface conductivity. Equation (33) can be considered as the Born approximation.[68]

Application of Born approximation (33) to an MWCNT allows us to express the axial surface current density $J_p(z)$ on the surface of the pth shell as

$$J_p(z) \approx \sigma_p E_z^{(0)}(R_p,z), \quad p \in [1,N]. \tag{34}$$

This expression can be justified as follows. The electric field exciting the pth shell is made of two components: (i) the electric field $\mathbf{E}^{(0)}$ incident on the entire MWCNT and (ii) the sum of the electric fields radiated to the surface current densities J_q, $q \in [1,N]$ but $q \neq p$. Equation (34) is justified if the first component is much larger than the second component at $\rho = R_p$, i.e., the condition

$$\left| \left(\frac{d^2}{dz^2} + k^2 \right) \Pi(R_p,z) \right| \ll |E_z^{(0)}(R_p,z)|,$$

$$z \in [-L/2, L/2], \quad p \in [1,N], \tag{35}$$

holds true. Substituting Eqs. (26) and (34) into Eq. (35), we arrive at the condition

$$\left| \sum_{q=1}^{N} R_q \sigma_q \int_{-L/2}^{L/2} E_z^{(0)}(R_q,z') G(z-z',R_p,R_q) dz' \right| \ll \left| \frac{c}{2} \int_{-L/2}^{L/2} E_z^{(0)}(R_p,z) \exp(ik|z-z'|) dz' \right|,$$

$$z \in [-L/2, L/2], \quad p \in [1,N], \tag{36}$$

for the applicability of the Born approximation. We found that condition (36) holds true for MWCNTs that are not too thick (i.e., R_N is sufficiently small) in the frequency regime wherein the surface conductivities σ_p, $p \in [1,N]$, are mostly determined by interband transitions. We estimate that MWCNTs with outermost radius $R_N < 20$ nm satisfy Eq. (34) at frequencies in the midinfrared and the visible regimes.

Equation (34) contradicts the edge conditions [Eq. (25)]. An analogous situation appears, for example, in the theory of diffraction by an aperture in an infinitesimally thin perfectly conducting screen, wherein the exact solution must satisfy the Meixner condition[66] on the aperture edge but an approximate solution based on the Huygens principle does not satisfy that condition. However, the error is strongly localized in the vicinity of the edge of the aperture and does not influence the scattered field in the far zone.[69] For our problem, Eq. (34) may be interpreted as a version of the Huygens principle for an MWCNT: the scattered field is generated by secondary current densities induced by the incident electric field on the surfaces of all shells. Therefore, the applicability of Eq. (34) is unphysical only in the vicinity of the edges $z = \pm L/2$, but that should not affect the performance of the MWCNT as an antenna in the interband-transition regime.

When the MWCNT is electrically thin in cross section ($kR_N \ll 1$), the further approximation

$$E_z^{(0)}(\rho,z) \simeq E_z^{(0)}(0,z), \quad \rho \leq R_N \tag{37}$$

is permissible. Then the substitution of Eq. (34) in Eqs. (31) and (32) yields

$$P_r = \frac{\omega^2 |\sigma_T|^2}{4c^3} \int_0^{\pi} \sin^3\theta \left| \int_{-L/2}^{L/2} e^{ikz\cos\theta} E_z^{(0)}(0,z) dz \right|^2 d\theta, \tag{38}$$

$$P_t = \frac{1}{2} \mathrm{Re}(\sigma_T) \int_{-L/2}^{L/2} |E_z^{(0)}(0,z)|^2 dz, \tag{39}$$

where

$$\sigma_T = \sum_{p=1}^{N} (2\pi R_p \sigma_p) \tag{40}$$

is the *effective* conductivity per unit length of an electrically thin MWCNT. Condition (36) leads to the inequality $P_t \gg P_r$; consequently,

$$\eta \approx P_r/P_t \sim |\sigma_T|^2/\mathrm{Re}(\sigma_T). \tag{41}$$

As determined by Eqs. (38) and (39), P_t and P_r are the same as for a thin-wire resistive antenna whose conductivity per unit length is equal to σ_T.[70] Thus, an electrically thin MWCNT which satisfies condition (36) may be modeled as a thin homogenous cylinder with conductivity per unit length determined from Eq. (40).

IV. NUMERICAL RESULTS

In order to present illustrative results, let us consider an MWCNT consisting of only zigzag shells. A large number of such MWCNTs are possible.[1,2] Moreover, after a suitable modification of EBCs (12) and (13),[71] the approach developed can be extended to MWCNTs comprising shells with arbitrary chirality vectors.

For definiteness, calculations were performed for two types of MWCNTs, hereafter referred to as type A and type M, shown in Fig. 3. The pth shell in an MWCNT of type A

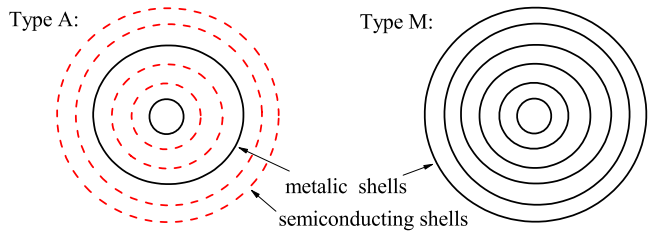

FIG. 3. (Color online) Schematics of MWCNTs of types A and M. All shells in an MWCNT of type M are metallic. In contrast, an MWCNT of type A contains a metallic shell alternating with two semiconducting shells.

is in the $(8p+1,0)$ configuration; hence, two consecutive semiconducting shells are followed by a metallic shell. The pth shell in an MWCNT of type M is in the $(9p,0)$ configuration; hence, all N shells are metallic. The radius of the pth shell is given by

$$R_p = \begin{cases} \sqrt{3}(8p+1)b/(2\pi), & \text{type A} \\ 9\sqrt{3}pb/(2\pi), & \text{type M}. \end{cases} \tag{42}$$

The frequency $f_p^{(1)}$ of the first interband transition for the pth shell of the metallic type is determined by the energy difference between the lowest van Hove singularity of the conducting band and the highest van Hove singularity of the valence band. Thus, an analysis of the dispersion equation for electrons in zigzag shells yields[48]

$$f_p^{(1)} \simeq \frac{v_F}{\mu_p \pi R_p}, \quad \mu_p = \begin{cases} 1, & \text{metallic shell} \\ 3, & \text{semiconducting shell}. \end{cases} \tag{43}$$

The frequency regime below the interband-transition regime for an MWCNT is dictated by the condition

$$f < f_e, \tag{44}$$

where

$$f_e = \min_p\{f_p^{(1)}\}, \tag{45}$$

while the condition

$$f > (2\pi\tau)^{-1} \tag{46}$$

establishes the frequency regime for long-range guided-wave propagation. As a result, the frequency regime wherein long-range guided waves can produce geometric (antenna) resonances is as follows:

$$(2\pi\tau)^{-1} \lesssim f \lesssim f_e. \tag{47}$$

At frequencies in the regime $f \gtrsim f_e$, the interband transitions contribute strongly to the surface conductivity of each shell such that the real and the imaginary parts of this quantity are approximately equal in magnitude. Guided waves then get attenuated heavily. At frequencies in the regime $f \lesssim 1/(2\pi\tau)$, attenuation of guided waves is caused by fast electron relaxation in all shells.

A. Azimuthally symmetric guided waves in an infinitely long MWCNT

Let us now examine azimuthally symmetric guided-wave propagation at $f=11.2$ THz in an infinitely long MWCNT of type A consisting of $N=13$ shells. The relaxation time τ is taken to be vanishingly small.

The shells numbered $p \in \{4,7,10,13\}$ are metallic. All interband transitions for these shells occur at frequencies exceeding 31 THz and therefore do not contribute to the effective conductivity (per unit length) of the MWCNT. The imaginary part of the surface conductivity of a metallic shell is positive valued and exceeds the real part in magnitude. Thus, the necessary condition for the long-range propagation of guided waves is satisfied.

The semiconducting shells labeled $p \in \{2,3,5,6\}$ have negligible surface conductivity and therefore do not influence the scattering properties of the chosen MWCNT at 11.2 THz. The surface conductivities of the semiconducting shells labeled $p \in \{8,9,11,12\}$ are dictated mainly by the corresponding first interband transitions occurring at $f_p^{(1)} \in \{36.5,32.5,26.7,24.4\}$ THz. At $f=11.2$ THz, the imaginary parts of the surface conductivities of these shells are negative and several times smaller than the surface conductivities of adjacent metallic shells. Therefore, the surface current densities in these semiconducting shells are smaller and oppositely directed with respect to their counterparts in adjacent metallic shells. The real parts of the surface conductivities of these semiconducting shells are high enough to cause large Ohmic losses.

We considered only the two eigenmodes of guided-wave propagation in the chosen MWCNT with the smallest retardation, labeled as $GW1$ and $GW2$. They correspond to the two roots of the dispersion equation, identified as h_1 and h_2, with the smallest real parts: $\mathrm{Re}(h_2) > \mathrm{Re}(h_1)$. Of all eigenmodes, these two will mostly influence the scattering properties of the finite-length MWCNT, as discussed in Sec. IV B.

The radial dependences of E_z and H_ϕ inside the MWCNT of type A for guided waves $GW1$ and $GW2$ are shown in Fig. 4(a). Clearly, the axial component of the electric field is distributed over the entire cross section of the MWCNT. The azimuthal component of the magnetic field is discontinuous across each metallic shell, in accordance with boundary condition (12). The degree of discontinuity decreases as the shell number p increases, in compliance with the generally decreasing magnitudes of J_p in Fig. 4(b). Outside the MWCNT, the radial distribution of the electric and magnetic fields is governed by the argument of the modified Bessel function $K_0(\kappa\rho)$, whereby we conclude that the electromagnetic field is highly localized to the MWCNT.

The axial surface current density J_p, $p \in [1,N]$, is shown in Fig. 4(b) for guided waves $GW1$ and $GW2$. In opposition to the radial distributions of the axial electric field, the magnitude of the current density is maximal on the innermost shell and then strongly decreases with the increase in the shell number p. This behavior is in agreement with the R^{-1} dependence of the surface conductivity of a metallic SWCNT of radius R.[4]

Figure 4(c) shows the radial distribution of the axial component of the time-averaged Poynting vector

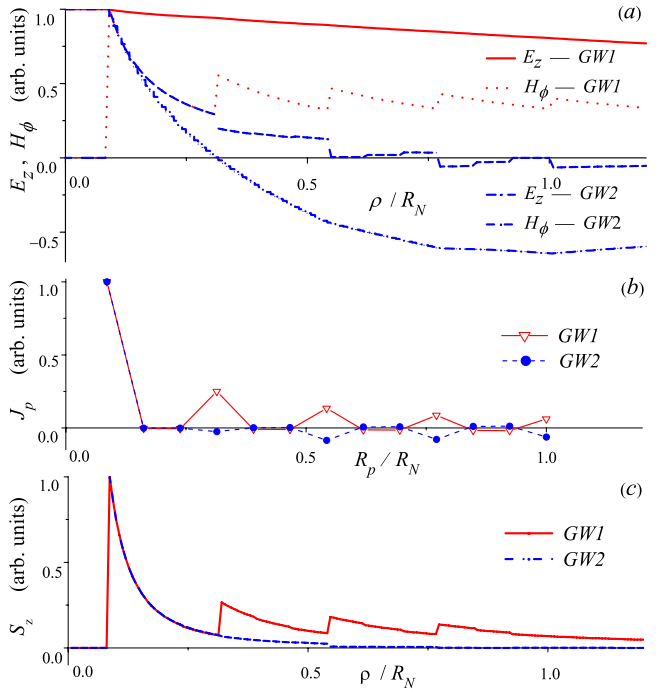

FIG. 4. (Color online) The radial dependencies of (a) E_z and H_ϕ, (b) J_p on the surfaces of the shells, and (c) the axial component of the time-averaged Poynting vector, for guided waves $GW1$ and $GW2$, in an MWCNT of type A with $N=13$ shells at $f=11.2$ THz, in the lim $\tau\to\infty$. The discrete points in (b), corresponding to different shells, are joined together only to aid the eyes.

$$S_z = \frac{c}{8\pi}\mathrm{Re}\left(\frac{h}{k}\right)|H_\phi|^2 \tag{48}$$

for $GW1$ and $GW2$ inside the MWCNT and in the vicinity of its outermost shell. The energy-flux density for $GW1$ is maximum near the surface of the innermost metallic shell and then slightly varies about some mean value between the 4th and the 13th shells. The energy-flux density for $GW2$ is mostly concentrated between the two innermost metallic shells and then decreases very rapidly as $\rho\to R_N$. Clearly then, the two innermost metallic shells are dominant contributors to the retardation of both $GW1$ and $GW2$.

The dependences of the real part of the slow-wave coefficient $\beta=k/h$ and the ratio $-\mathrm{Re}(\beta)/\mathrm{Im}(\beta)=\mathrm{Re}(h)/\mathrm{Im}(h)$ of the guided waves $GW1$ and $GW2$ on the number N of shells in MWCNTs of types A and M are shown in Fig. 5. The retardation coefficient $\mathrm{Re}(\beta)$ for MWCNTs of type M is higher than for MWCNTs of type A of comparable R_N, which is a significant observation in relation to the geometric resonances of finite-length MWCNTs (Sec. IV B).

For MWCNTs of type M, $\mathrm{Re}(\beta)$ increases as N does. As N increases, the additional outmost shell has a lower influence on $\mathrm{Re}(\beta)$. The increase in $\mathrm{Re}(\beta)$ with increasing N occurs until R_N exceeds $v_F/\pi f$, per conditions (43) and (47).

Figure 5(a) shows that, for guided waves $GW1$ and $GW2$ in MWCNTs of type A, $\mathrm{Re}(\beta)$ (i) increases with the addition of a metallic shell but (ii) decreases with the addition of a semiconducting shell. For an MWCNT with small N, $\mathrm{Re}(\beta)$ is thus determined mostly by the metallic shells. In contrast,

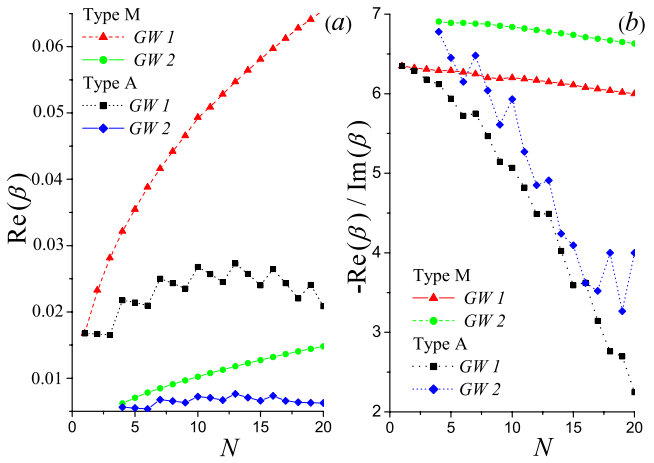

FIG. 5. (Color online) Dependences of (a) $\mathrm{Re}(\beta)$ and (b) $-\mathrm{Im}(\beta)/\mathrm{Re}(\beta)$ on N for guided waves $GW1$ and $GW2$ in MWCNTs of types A and M, when $f=11.2$ THz and $\tau=10^{-13}$ s. Discrete points are joined by lines to aid the eyes.

for MWCNTs with large N, both $\mathrm{Re}(\beta)$ and $-\mathrm{Re}(\beta)/\mathrm{Im}(\beta)$ are strongly affected by the semiconducting shells of large radius. This occurs because the semiconducting shells labeled $p\in\{11,12,14,15,17,18,20\}$ have their first interband transitions near the chosen frequency of 11.2 THz, and, consequently, the real and imaginary parts of their surface conductivities are large in magnitude. An increase in the number of such shells greatly diminishes the parameters $\mathrm{Re}(\beta)$ and $-\mathrm{Re}(\beta)/\mathrm{Im}(\beta)$ of $GW1$ and $GW2$ in the MWCNTs of type A. Thus, *interband transitions* suppress guided-wave propagation in MWCNTs.

B. Scattering properties of a finite-length MWCNT

Let us now move on to the scattering properties of finite-length MWCNTs in the terahertz and the far-infrared frequency regimes. Here we focus only on the case when the incident electric field is parallel to the z axis, thereby permitting us to investigate electromagnetic effects caused by the axial surface conductivities of the shells.

Figure 6(a) illustrates the frequency dependence of the imaginary part of the polarizability scalar α_{zz} in the long-wavelength regime ($kL\ll 1$) for different lengths L and shell numbers N in MWCNTs of types A and M. The labels $GS1$ and $GS2$ in this figure denote the first geometric resonance of the guided waves $GW1$ and $GW2$, respectively. The geometric resonances occur at frequencies[16,33]

$$f_s \simeq s\left(\frac{c}{2L}\right)\mathrm{Re}(\beta), \quad s\in\{1,3,5,\ldots\}. \tag{49}$$

Equation (49) provides a simple estimate of the geometric-resonance frequencies. For a better estimate, the correction factor accounting for the phase shift of the guided wave reflected from the CNT edge must be introduced in Eq. (49) by analogy with macroscopic wire antennas.[51] For calculating this factor, the integral-equation technique can be applied.

As we concluded from Fig. 5(a), the retardation coefficient $\mathrm{Re}(\beta)$ for MWCNTs of type M is higher than for

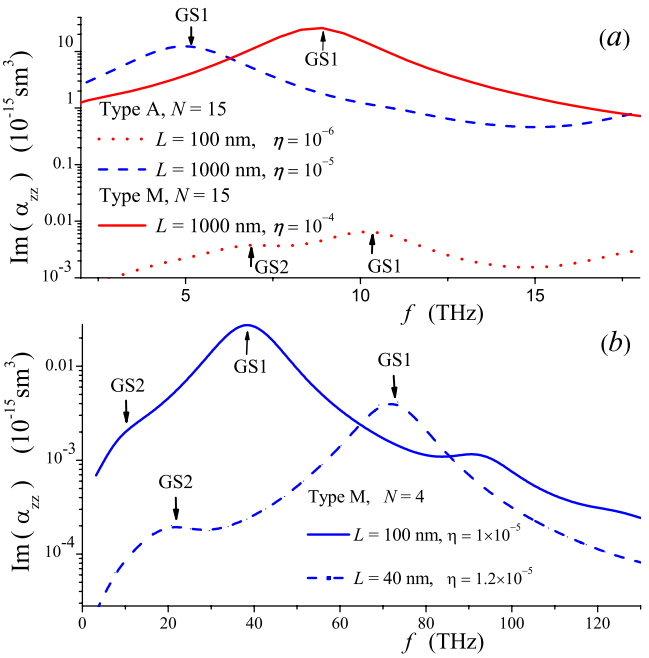

FIG. 6. (Color online) Frequency dependence of $\mathrm{Im}(\alpha_{zz})$ of MWCNTs of types A and M for different lengths L and number of shells N. The labels $GS1$ and $GS2$ denote the first geometric resonance—$s=1$ in Eq. (49)—of the guided waves $GW1$ and $GW2$, respectively. (a) $\tau=10^{-13}$ s; (b) $\tau=2\times10^{-14}$ s.

MWCNTs of type A of comparable R_N. Therefore the first geometric resonance ($s=1$) for the MWCNTs of type M appears in Fig. 6(a) at a higher frequency than for MWCNTs of type A, both of the same length L.

The resonance frequencies for $GW1$ and $GW2$ depend on L nonlinearly. As an example, in Fig. 6(a) the resonance frequency of the MWCNT of type A increases by a factor of about 2 (from 5 to ~10 THz) while the length L decreases by a factor of 10 (from 1000 to 100 nm). That is reflected in Eq. (49) by the strong dependence of $\mathrm{Re}(\beta)$ on f when f is close to f_e. Accordingly, the dependence of the frequency of the geometric resonance on L is not explicit.

The first resonance of the MWCNT of type A and length $L=100$ nm at ~10 THz frequency is not strong because condition (47) is not satisfied for this MWCNT, and the guided wave is strongly attenuated. We conclude that the resonance of an MWCNT antenna of type A or M near a given frequency is the most pronounced if both Eqs. (47) and (49) are satisfied.

Figure 6(a) contains the value of the antenna efficiency η at the first geometric resonance for all MWCNTs considered. This antenna efficiency depends both on the type and the length of the MWCNT. The antenna efficiency of an MWCNT is several times larger than that of an SWCNT of the same length. Our calculations make us conclude that the restrictions on the MWCNT dimensions given by Eqs. (47) and (49) do not permit an increase in η at the first geometric resonance. In contrast, the antenna efficiency of an almost circular bundle of closely packed SWCNTs can be increased up to unity by increasing of number of metallic SWCNTs in the bundle.[33]

When conduction in an MWCNT is very diffuse,[72] the relaxation time τ is close to that for graphite (2×10^{-14} s). Then conditions (47) and (49) can be fulfilled only for MWCNTs of type M and that too with $R_N \lesssim 2.5$ nm and $L \lesssim 200$ nm. Figure 6(b) shows the frequency dependence of $\mathrm{Im}(\alpha_{zz})$ of an MWCNT of type M with $N=4$ for $\tau=2\times10^{-14}$ s. The first geometric resonances of MWCNTs of lengths $L=100$ nm and $L=40$ nm appear in the far-infrared ($f=38$ THz) and the midinfrared ($f=72$ THz) regimes, respectively. Thus, antenna resonances are pronounced and can be experimentally observed for short MWCNTs with several shells only in the far-infrared and midinfrared regimes.

C. MWCNT properties in the interband-transition regime

Whereas Secs. IV A and IV B address the frequency regime $f \in (1/2\pi\tau, f_e)$ wherein interband transitions are not possible, we now proceed to the interband-transition regime of Sec. III B, wherein the electromagnetic response properties of MWCNTs are dominated by the interband transitions. This regime, delineated by the condition $f > f_e$, can very well lie in the visible part of the electromagnetic spectrum.

The description of an MWCNT as an antenna was initiated by Hao and Hanson.[32] They showed that modeling a finite-length MWCNT as a single cylindrical shell with typical surface conductivity scalar—given, e.g., in Ref. 4—cannot produce a *length-matching* antenna effect in the visible regime. The reason is the low surface conductivity of the MWCNT shells.[4] In the Hao-Hanson model,[32] however, the intershell electromagnetic coupling in the MWCNT was ignored, which is inappropriate if $R_N \gtrsim 20$ nm, as we pointed out in Sec. III B.

The lacuna in the Hao-Hanson model[32] can be removed by implementing the integral-equation technique of Sec. III A. Therefore, we decided to examine the scattering properties of finite-length MWCNTs of radius $R_N \simeq 25$ nm and $R_N \simeq 50$ nm in the visible regime, taking the intershell electromagnetic coupling into account (but ignoring the intershell electron tunneling). As we discuss later in this section, our analysis confirmed the absence of the length-matching antenna effect in the near-infrared and the visible regimes.

Let us first analyze the effective conductivity per unit length of an electrically thin MWCNT, as estimated by Eq. (40). Figure 7(a) presents the real part of σ_T as a function of N for MWCNTs in the near-infrared and the visible regimes. This figure shows that, for SWCNTs ($N=1$) and MWCNTs with $N \in [2,4]$, σ_T has strong resonances. The resonances weaken as N increases and practically disappear for $N>10$. This trend can be explained in the following way. In the near-infrared and the visible regimes, the surface conductivity σ_p of the pth shell has many resonances corresponding to van Hove singularities. As the resonances of different shells overlap, the weighted summation of the surface conductivities of all shells in Eq. (40) ensures that σ_T does not evince resonant behavior in the near-infrared and the visible regimes.

The conductivity per unit length of an isolated shell of radius $R_p \gtrsim 5$ nm also has a large number of closely spaced resonances so that, instead of discrete lines, a band appears in its spectrum. As the surface conductivities of all MWCNT shells have a plasmon resonance[61] in the ultraviolet regime at

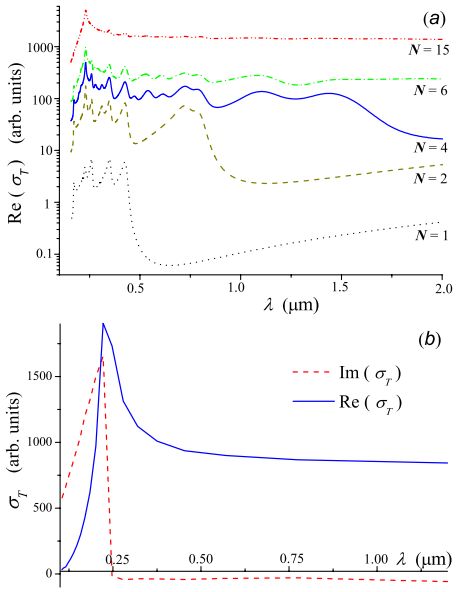

FIG. 7. (Color online) (a) Real part of the effective conductivity per unit length of an MWCNT of type M in the near-infrared and the visible regimes. The number N is variable and $\tau=2\times10^{-14}$ s. Note that $R_{15}=5.284$ nm. (b) Real and imaginary parts of σ_T of an MWCNT of type M with $N=29$ shells in the near-infrared and the visible regimes.

the free-space wavelength $\lambda_{pl}=(c\pi\hbar)/\gamma_0$, σ_T for any MWCNT also has a resonance at this wavelength.

The real and imaginary parts of the effective per-unit-length conductivity σ_T for an MWCNT of type M with $N=29$ shells (i.e., $R_N=10.22$ nm) are presented in Fig. 7(b). As this figure demonstrates, the real part of σ_T increases as the frequency increases and has a maximum near $f=1304$ THz (i.e., $\lambda=230$ nm), which is not a geometric-resonance frequency but, instead, is a plasmon-resonance frequency.[61] In the near-infrared and the visible regimes, the condition $\mathrm{Re}(\sigma_T)\gg\mathrm{Im}(\sigma_T)$ holds; therefore, the chosen MWCNT cannot support surface-wave propagation, which occurs for a metallic wire with $\mathrm{Re}(\sigma)\ll\mathrm{Im}(\sigma)$ according to Ref. 73. We also found that the electric field exciting a particular shell differs very slightly from the electric field incident on the MWCNT when $R_N\lesssim20$ nm and the frequency

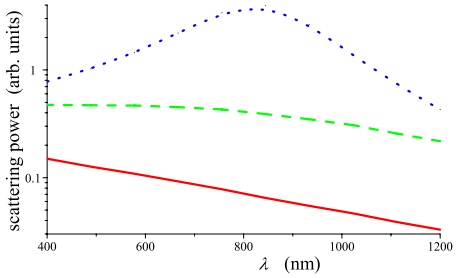

FIG. 8. (Color online) Scattered power P_r versus free-space wavelength λ for MWCNTs with $N=70$ (solid line) and $N=140$ shells (dashed line) and length $L=350$ nm; $\tau=2\times10^{-14}$ s. The scattered power for a perfectly conducting rod (dotted line) of cross-sectional radius 25 nm and length 350 nm was calculated by solving Eq. (28) with $N=1$ and $\sigma_1\to\infty$.

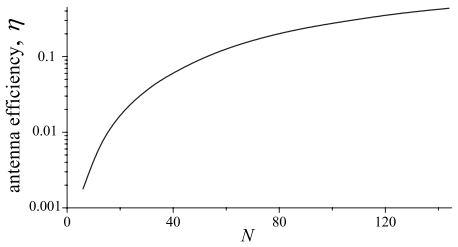

FIG. 9. Dependence of the antenna efficiency η on the number N of shells in an MWCNT of type M and length $L=350$ nm at frequency $f=600$ THz (visible regime); $\tau=2\times10^{-14}$ s.

lies in either the near-infrared or the visible regimes, thereby implying that the electromagnetic coupling between the shells is slight. The frequency dependence of the scattering power P_t for such an MWCNT is the same as of $|\sigma_T(\omega)|^2$, according to Eq. (38).

Let us now carry on to electrically thick MWCNTs (with $R_N\simeq25$ or 50 nm). For calculation of the electric current densities in their shells in the near-infrared and the visible regimes we used Eq. (28), with $E_z^{(0)}(\rho,z)$ assumed to be independent of $\rho\in[0,R_N]$. Such an approximation is sufficient to ascertain whether geometric resonances of azimuthally symmetric modes exist in thick MWCNTs or not. Of course, σ_T cannot be defined for electrically thick MWCNTs.

In the near-infrared and the visible regimes, the surface conductivity of a shell of large radius ($R\gtrsim5$ nm) does not depend on that whether shell is metallic or semiconducting. Therefore, though the plots in Figs. 8–10 were made for thick MWCNTs of type M, all results presented therein are qualitatively true for thick MWCNTs of type A also.

In order to compare the electromagnetic responses of the chosen MWCNTs and a perfectly conducting rod in the near-infrared and the visible regimes, we need to calculate the

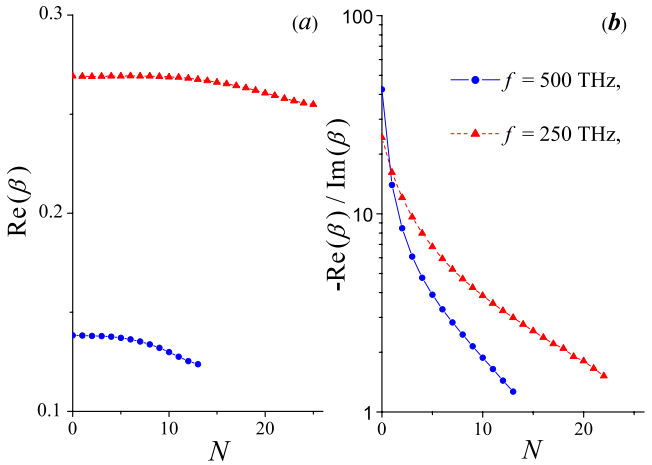

FIG. 10. (Color online) Dependences of (a) $\mathrm{Re}(\beta)$ and (b) the ratio $-\mathrm{Re}(\beta)/\mathrm{Im}(\beta)$ on the number N of carbon shells for a surface-plasmon wave in an MWCNT with a gold core. The MWCNT is of type M, and its pth shell has a $(90+9p,0)$ zigzag configuration and radius $R_p=\sqrt{3}(90+9p)b/(2\pi)$, $p\in[1,N]$. The gold core has a cross-sectional radius $R_0=3.5$ nm and $\tau=2\times10^{-14}$ s. Data for an isolated metal wire of cross-sectional radius R_0 is the same as for $N=0$. Discrete points are joined by lines to aid the eyes.

scattered power P_r when the incident electric field is oriented parallel to the z axis. When we calculated the scattered power P_r for MWCNTs of type M, length $L=350$ nm, and $N=70$ ($R_N=24.66$ nm) or $N=140$ ($R_N=49.32$ nm), resonances did not show up for $f\in[250,750]$ THz (i.e., $\lambda\in[400,1200]$ nm) in Fig. 8. For comparison, the scattered power for a perfectly conducting rod of cross-sectional radius 25 nm and length 350 nm is also shown in Fig. 8. This nanorod antenna, in contrast to the MWCNTs, has a set of resonances determined by the condition

$$L=\kappa s\lambda/2, \quad s\in\{1,2,3,\cdots\}, \tag{50}$$

where κ is a correction factor that slightly exceeds unity and is a function of the ratio of the length and the wavelength as well as of the ratio of cross-sectional radius and the length.[51] For the chosen nanorod antenna, the first resonance ($s=1$) is characterized by $\kappa=1.15$ and appears at $f=370$ THz (i.e., $\lambda=810$) nm, which is confirmed by the dotted line in Fig. 8.

The absence of antenna (geometric) resonances of the chosen MWCNTs in the visible regime can be explained by the strong dissipation of electromagnetic energy in MWCNT shells and the small electromagnetic coupling between the shells, as discussed in Sec. III B. Therefore, even an MWCNT with $R_N\simeq 50$ nm and comprising 140 shells cannot support guided-wave propagation and, consequently, cannot display the length-matching antenna effect. The same conclusion is also true in the visible regime for SWCNTs (Ref. 16) and planar arrays of finite-length SWCNTs.[32] Let us remark that a hypothetic multishell conductive structure with $N=70$ and $R_N\simeq 25$ nm can have an antenna resonance corresponding to $s=1$ in Eq. (50), provided the surface conductivity of every shell is five times that given in Ref. 4; but such a structure has not been practically realized as yet.

The dependence of the antenna efficiency η in the visible regime on the number N of shells in the MWCNT is illustrated in Fig. 9. The antenna efficiency increases with the number of shells and tends to unity for thick MWCNTs; indeed, $f=600$ THz, we calculated $\eta=0.17$ for $N=70$, but $\eta=0.44$ for $N=140$.

D. Surface-plasmon-wave propagation in an MWCNT with a gold core

These days, thin metallic (gold, silver, and aluminum) wires of finite length are considered to be promising for application as optical nanoantennas.[54,74] However, the fabrication of long, high-quality, thin, single-crystal wires of cross-sectional radius less than 5 nm and with perfect cylindrical form (i.e., without breaks, bends, deformations, etc.) is a difficult technological problem. Recently, CNTs have been used as templates in order to promote the formation of high-quality single-crystal wires coated by perfect graphene cylinders.[75] This is an exciting possibility for a composite nanoantenna comprising a solid metallic core covered by concentric carbon shells. Clearly, such a structure is neither a metallic cylinder nor an isolated MWCNT.

Surface-plasmon waves in the infrared and the visible regimes can propagate along a metal wire.[73] Surely, guided-wave propagation would be affected if the metallic wire was to be enclosed in an ensemble of concentric carbon shells. The theoretical approach of Sec. II B can be applied to study the phenomenon of surface-plasmon waves as follows.

Suppose that the metal core is of cross-sectional radius $R_0<R_1$, the radius of the innermost shell of an MWCNT. If R_0 is much less than the skin depth of the bulk metal and $kR_0\ll 1$, then the metal core can be modeled as a solid cylinder with surface conductivity $\sigma_0=\sigma_{\text{met}}R_0/2$,[76] where σ_{met} is the bulk volumetric conductivity of the metal. Also, R_0 has to be higher than a critical value R_{cr}, which corresponds to the crystalline–noncrystalline transition in metals and separates the quasibulk behavior ($R_0>R_{\text{cr}}$) from the quasimolecular behavior ($R_0<R_{\text{cr}}$) of a nanowire. Then, Eqs. (12)–(14) also hold at $\rho=R_0$ with $\sigma_p\to\sigma_0$ and the procedures of Sec. II B are applicable.

We considered the propagation of surface-plasmon waves in an MWCNT with a gold core. The bulk volumetric conductivity σ_{met} of gold was taken to follow the Drude model with parameters given in Ref. 77. The skin depth of gold in the visible regime is higher than 30 nm. The value $R_{\text{cr}}=1.5$ nm for gold was obtained with first-principles calculations in Ref. 78. So we assumed that $1.5\ \text{nm}<R_0\ll 30$ nm.

Figure 10 presents the dependences of $\text{Re}(\beta)$ and $-\text{Re}(\beta)/\text{Im}(\beta)$ of a surface-plasmon wave on the number N of shells in MWCNT of type M with a gold core of cross-sectional radius $R_0=3.5$ nm. The pth shell of the MWCNT has a $(90+9p,0)$ zigzag configuration and radius $R_p=\sqrt{3}(90+9p)b/(2\pi)$, $p\in[1,N]$. In the near-infrared ($f=250$ THz) and the visible ($f=500$ THz) regimes, Fig. 10(a) shows that the retardation coefficient $\text{Re}(\beta)$ depends only slightly on N. According to Fig. 10(b), the value of $-\text{Re}(\beta)/\text{Im}(\beta)$ is less than for an isolated metal wire ($N=0$) and significantly decreases as N increases.

These trends can be explained in the following manner. The guided wave propagates partly inside the MWCNT and partly inside the gold core. The dissipation in the MWCNT shells is high because the real and the imaginary parts of the surface conductivities of the shells in the interband regime are of comparable magnitudes. This dissipation increases with frequency, in accordance with the frequency dependence of the effective per-unit-length conductivity of the MWCNT presented in Fig. 7(b). Because of the weak electromagnetic coupling of CNT shells, the shells strongly absorb electromagnetic energy independently on each other—which explains the strong dependence of $-\text{Re}(\beta)/\text{Im}(\beta)$ on N. Furthermore, the weak coupling changes the radial electromagnetic field distribution of the surface-plasmon wave only slightly as N increases, which explains the weak dependence of $\text{Re}(\beta)$ on N.

The decrease in the magnitude of $-\text{Re}(\beta)/\text{Im}(\beta)$ with increasing N implies the enhancement of P_t, the power lost to Ohmic dissipation, and consequently the decrease in the antenna efficiency η of an MWCNT with a metal core. However, if N is not too large ($N=2$ or 3) some worsening of antenna properties may be justified by other advantages that the metal-core MWCNT may confer.

V. DISCUSSION

Thus, an MWCNT can operate as an antenna in two different regimes. The first is the *Drude-conductivity regime*,

wherein the motion of conduction-band electrons is responsible for radiation properties. This regime has a distinct analogy with a classical radio-frequency wire antenna, as is clear from Secs. III B and IV B. The second regime is the *interband-transition regime*, wherein quantum transitions of electrons between different energy states occur. This regime was considered in Sec. IV C and does not have a classical analogy. The frequency f_e separates the Drude-conductivity regime $f \in (1/2\pi\tau, f_e)$ from the interband-transition regime $f > f_e$.

Guided-wave propagation and geometric resonances of the guided waves are typical for macroscopic wire antennas. The guided waves have a quasitransverse-electromagnetic structure and are characterized by low retardation and low attenuation.[51] The existence of guided (surface) waves and geometric resonances also is typical for nanowire antennas in the Drude-conductivity regime.[4,16,74] But the guided wave has strong retardation and high attenuation, so that the frequency of a geometric resonance is not connected to the free-space wavelength but to a shorter effective wavelength that depends on the material properties.[54] This general rule is also true for MWCNT antennas: Fig. 5 shows that guided waves have strong retardation and high attenuation, and Fig. 6 presents geometric resonances at $\lambda \ll L$ demonstrating thereby the effective wavelength to be shorter than free-space wavelength.

Calculated data presented in Fig. 5(a) indicate that the retardation coefficient increases when the number of shells increases. Furthermore, the retardation coefficient is the highest for the $GW1$ mode in MWCNTs of type M. That implies that an MWCNT with only metallic shells and operating in the $GW1$ mode offers attractive prospects for high antenna efficiencies in the terahertz regime.

The frequency f_e, separating the Drude-conductivity regime from the interband-transition regime, depends on the detailed electronic and geometric attributes of the MWCNT. According to Eq. (43), f_e decreases as R_N increases. As examples, for an MWCNT of type A, (i) $R_N=10$ nm and $f_e=9.3$ THz when $N=32$, but (ii) $R_N=1.9$ nm and $f_e=48$ THz when $N=6$. In the interband-transition regime $f > f_e$, guided-wave propagation and geometric resonances are absent for both SWCNTs and MWCNTs, which cardinally distinguish this regime from the Drude-conductivity regime.

As shown experimentally,[79] the absorption and the scattering characteristics of an electrically thick MWCNT in the regime of optical transitions depend only slightly on the frequency. This conclusion, also borne out by the data in Fig. 8, may seem to be unexpected. In fact, optical transitions are resonance processes and the surface conductivities of SWCNTs and MWCNT shells have resonances corresponding to the van Hove singularities. But we found that the antenna parameters of electrically thin MWCNTs are determined by the effective parameter σ_T defined in Eq. (40). The overlapping of a large number of resonances of the surface conductivities of the different shells leads to a smooth frequency dependence of σ_T. Such an effect is analogous to inhomogeneous broadening in an ensemble of all different harmonic oscillators.[80]

Antennas are objects that transform a near field into a far field and vice versa. The morphology of the near field of a nanoantenna possesses a nanoscale and is therefore determined by quantum size effects. Therefore the coupling of a nanoantenna with its near field is stronger than that of a macroscopic antenna with its near field; as a result, the transformation of the near field to the far field by a nanoantenna is more difficult, and the antenna efficiency of a thin-nanowire antenna is low. This property is inherent to different types of nanoantennas: SWCNTs,[14,15] bundles of SWCNTs,[33] metallic nanorods,[19] and MWCNTs as in Fig. 6. The antenna efficiency can be enhanced by increasing the number of shells in an MWCNT (Fig. 9), the number of SWCNTs in a bundle (Fig. 7 in Ref. 33), and the cross-sectional radius of a metallic rod antenna (Fig. 1 in Ref. 19). We can thus conclude that a small value of the antenna efficiency is the fundamental physical characteristic of nanoantennas. Nevertheless, the antenna efficiency is tunable over a wide range.

In order to achieve antenna efficiency close to unity, it is necessary to strongly suppress the influence of quantum size effects by ensuring that the cross-sectional radius is high. Note that, since quantum size effects are not pronounced in gold nanowires of cross-sectional radius of several tens of nanometers, such nanowire-based antennas are expected to possess properties analogous to macroscopic antennas.

The electromagnetic properties of MWCNTs have only a slight frequency dependence in the interband-transition regime, per Fig. 8. Thus, and MWCNT can be considered to be a nanoantenna with sufficiently high η (≈ 0.1 in Fig. 9) and a wide operating-frequency range in the visible regime. Such nanoantennas have properties similar to those of electrically small but macroscopic antennas in microwave regimes (e.g., short nonresonant dipoles).[51]

VI. CONCLUDING REMARKS

To conclude, we modeled the shells of an MWCNT as impedance sheets with axially directed surface conductivity. Intershell tunneling of electrons in a DWCNT was considered in detail. We showed that intershell tunneling leads to qualitatively different features in guided-wave propagation. The following conclusions emerged from our studies:

(i) Intershell tunneling qualitatively changes the form of EBCs in a DWCNT, in comparison to SWCNTs. The surface current densities and the axial component of the electric field on the surfaces of different shells get coupled, which effect leads to a generalized susceptibility that contains the mutual surface conductivities of both shells. The mutual surface conductivities are caused by the tunneling and are distinguished by strong axial nonlocality.

(ii) The existence of mutual conductivities leads to the appearance of electrostatic longitudinal waves in the spectra of a DWCNT. Two electrostatic modes exist: one characterized by normal dispersion and the other by anomalous dispersion.

(iii) Different types of guided waves in the DWCNT arise from intershell tunneling. The intershell tunneling practically does not influence the dispersion characteristics of symmetriclike waves, except in a narrow vicinity of the tunneling resonance. The dispersion characteristics of asymmetriclike waves are strongly affected in the wide frequency range by intershell tunneling.

When an MWCNT is excited by an incident electromagnetic field, the contributions of electrostatic and asymmetriclike guided waves to the electromagnetic response of the MWCNT are negligible. That permits to investigate the MWCNT antenna effects while neglecting intershell tunneling.

Calculated data indicate that in a low-frequency regime called the Drude-conductivity regime, wherein optical interband transitions do not occur, guided waves can propagate with low attenuation in an MWCNT which has metallic shells. In the same frequency regime, the axial polarizability of a finite-length MWCNT has a resonant behavior due to the antenna-length matching effect. However, the shells with surface conductivity due to interband transitions suppress guided-wave propagation. Due of the high dissipation in such shells, MWCNTs with outermost radius ≈ 25 nm cannot possess resonant properties in the visible regime. Analysis of surface-plasmon-wave propagation in an MWCNT with a gold core shows that, in the near-infrared and the visible regimes, the shells behave effectively as lossy dielectric materials and suppress surface-wave propagation along the gold core.

The following conclusions regarding the operation of MWCNTs as nanoantennas emerged from our work:

(i) The antenna efficiency η of an MWCNT exceeds that of an SWCNT but is less than that of an almost circular bundle of closely packed metallic SWCNTs, provided that all three objects are of roughly the same outermost radius. Therefore, SWCNT bundles are the most promising candidates for terahertz and midinfrared antennas.

(ii) An MWCNT with at least four shells is recommended for application as a nanoantenna with a wide operating-frequency range in the visible regime.

(iii) Filling the core of an MWCNT with a metal makes the MWCNT attractive as a nanoantenna, provided that the number of shells does not exceed 3.

ACKNOWLEDGMENTS

This research was partially supported by INTAS under Projects No. 05-1000008-7801 and No. 06-1000013-9225, International Bureau BMBF (Germany) under Project No. BLR 08/001, and Belarus Republican Foundation for Fundamental Research and CNRS (France) under Project No. F07F-013. M.V.S. thanks the World Federation of Scientists. A.L. acknowledges the Charles Godfrey Binder Professorship Endowment at the Pennsylvania State University for partial support.

APPENDIX A: DENSITY MATRIX AND DENSITY OF INDUCED CHARGE IN A DWCNT

The one-electron state $|\alpha_p\rangle=\{\tilde{\lambda},p_z,s\}_p$, $p\in\{1,2\}$, discussed in Sec. II A, has the form of a Bloch wave. Thus,[5]

$$|\alpha_p\rangle = \psi_\alpha(\mathbf{r}_j)e^{i(p_z z/\hbar+s\phi)}, \tag{A1}$$

where $\psi_\alpha(\mathbf{r})=\psi_\alpha(\mathbf{r}+\mathbf{R})$ is the periodic amplitude for the plane two-dimensional (2D) hexagonal lattice and $\mathbf{R}$ is the lattice vector. In the tight-binding approximation, the function $\psi_\alpha(\mathbf{r})$ has been presented in Ref. 5.

Let the DWCNT interact with an azimuthally symmetric electromagnetic field characterized by the electric potential $\mathcal{V}(\mathbf{r},t)$. The Hamiltonian of the interaction with electromagnetic field is $\hat{\mathcal{H}}_I=e\mathcal{V}(\mathbf{r},t)\hat{I}$, where $\hat{I}$ is the identity matrix. The whole Hamiltonian is $\hat{\mathcal{H}}=\hat{\mathcal{H}}_0+\Delta\hat{\mathcal{H}}+\hat{\mathcal{H}}_I$.

Let the electromagnetic field be adiabatically switched on at time t_s such that $t_s\to-\infty$. The field is weak enough for $\hat{\mathcal{H}}_I$ to be considered as a small perturbation. The azimuthally symmetric electric potential induces the azimuthally symmetric charge density n_{Sp} on the pth shell, $p\in\{1,2\}$. Let $\mathcal{V}$ and n_{Sp} be represented by the Fourier integrals,

$$\begin{Bmatrix}\mathcal{V}(\rho,z,t)\\ n_{Sp}(z,t)\end{Bmatrix} = \frac{1}{4\pi^2}\int_{-\infty}^{\infty}\int_{-\infty}^{\infty} e^{i(hz-\omega t)}\begin{Bmatrix}V(\rho,h,\omega)\\ n_{Sp}(h,\omega)\end{Bmatrix} dhd\omega. \tag{A2}$$

Analogously to $|\alpha_p\rangle$, we discuss also a one-electron state $|\alpha_p'\rangle=\{\tilde{\lambda}',p_z+\hbar h,s+l\}_p$, where $l\in\{0,\pm1\pm2,\ldots\}$. Wave function (A1) is strongly localized in the shell vicinity. Therefore, the overlap between the wave functions belonging to the different shells can be neglected, and the orthogonality relation $\langle\alpha_{p'}'|\alpha_p\rangle\cong\delta_{pp'}\delta_{\alpha\alpha'}$ assumed to hold true.

The eigenstates $|\tilde{\alpha}\rangle$ of the Hamiltonian $\hat{\mathcal{H}}_0+\Delta\hat{\mathcal{H}}$ are determined by the equation $(\hat{\mathcal{H}}_0+\Delta\hat{\mathcal{H}})|\tilde{\alpha}\rangle=\mathcal{E}_{\tilde{\alpha}}|\tilde{\alpha}\rangle$. They are characterized by four variables $|\tilde{\alpha}\rangle=\{\tilde{\lambda},\zeta,p_z,s\}$, $\zeta\in\{1,2\}$, and can be represented as

$$|\tilde{\alpha}\rangle = \frac{1}{\sqrt{2}}(|\alpha_1\rangle + n_\zeta|\alpha_2\rangle) \tag{A3}$$

with the associated eigenenergy

$$\mathcal{E}_{\tilde{\alpha}} = \mathcal{E}_\alpha + n_\zeta N_{\tilde{\lambda}}\hbar\omega_t, \tag{A4}$$

where $n_1=1$ and $n_2=-1$.[81]

According to Eq. (A4), tunneling splits both the valence and conduction bands of each shell into two subbands indexed by ζ. The contribution of transverse motion of electrons to the axial conductivity is small enough that we can ignore all eigenstates with $l\neq0$. Then we can use the density matrix,

$$\hat{\rho}=\hat{\rho}(\mathbf{r}_1,\mathbf{r}_2)=\sum_{\tilde{\alpha}\tilde{\alpha}'}\rho_{\tilde{\alpha}\tilde{\alpha}'}|\tilde{\alpha}\rangle\langle\tilde{\alpha}'|, \tag{A5}$$

where $|\tilde{\alpha}'\rangle=\{\tilde{\lambda}',\zeta',p_z+\hbar h,s\}$. The initial state of the system is equilibrium as $t\to-\infty$, that is,

$$\lim_{t\to-\infty}\hat{\rho}|\tilde{\alpha}\rangle=\hat{\rho}_0|\tilde{\alpha}\rangle=F(\mathcal{E}_{\tilde{\alpha}})|\tilde{\alpha}\rangle, \tag{A6}$$

where $\hat{\rho}_0$ is the unperturbed density operator and $F(\mathcal{E})$ is the equilibrium Fermi distribution function.

Next, let us solve the Liouville equation $i\hbar\partial_t\hat{\rho}=\hat{\mathcal{H}}\hat{\rho}-\hat{\rho}\hat{\mathcal{H}}$ with initial condition (A6). We seek a solution in the form of $\hat{\rho}=\hat{\rho}_0+\delta\hat{\rho}$ with $\hat{\rho}_0$ determined from Eq. (A6) and $\delta\hat{\rho}$ as a small correction, determined by interaction with electromagnetic field. A standard perturbation method[5] yields

$$\delta\rho_{\tilde{\alpha}\tilde{\alpha}'}(h,\omega)=\frac{e[F(\mathcal{E}_{\tilde{\alpha}'})-F(E_{\tilde{\alpha}})](V_1+n_\zeta n_{\zeta'}V_2)M_{\alpha\alpha'}}{4\pi^2(\mathcal{E}_{\tilde{\alpha}'}-E_{\tilde{\alpha}}-\hbar\omega-i0)}e^{-i\omega t}, \tag{A7}$$

where $V_p=V(R_p,h,\omega)$, $p\in\{1,2\}$, and $M_{\alpha\alpha'}=\langle\alpha'|e^{-ihz}|\alpha\rangle$ is the normalized matrix element of the dipole transition between conduction and valence bands.[5] Accordingly to the assumptions made in Sec. II A, the matrix elements $M_{\alpha\alpha'}$ belonging to different shells are identical.

The induced charge density on the first shell can be evaluated as

$$n_{S1}(h,\omega)=2\sum_{\tilde{\alpha}\tilde{\alpha}'}\delta\rho_{\tilde{\alpha}\tilde{\alpha}'}M^*_{\alpha\alpha'}e^{i\omega t}. \tag{A8}$$

The factor 2 here is due to the spin degeneracy of π electrons. Substituting Eq. (A7) in Eq. (A8), we obtain

$$\begin{aligned}n_{S1}(h,\omega)=&\frac{e}{4\pi^2\hbar R_1}\sum_{\zeta\zeta'}(V_1+n_\zeta n_{\zeta'}V_2)\\&\times\sum_{\tilde{\lambda}\tilde{\lambda}'}\sum_s\int_{1\text{stBZ}}dp_z|M_{\alpha\alpha'}|^2\\&\times\frac{F(\mathcal{E}_{\alpha'}+N_{\tilde{\lambda}'}n_{\zeta'}\hbar\omega_t)-F(E_\alpha+N_{\tilde{\lambda}}n_\zeta\hbar\omega_t)}{E_{\alpha'}-\mathcal{E}_\alpha+(N_{\tilde{\lambda}'}n_{\zeta'}-N_{\tilde{\lambda}}n_\zeta)\hbar\omega_t-\hbar\omega-i0},\end{aligned} \tag{A9}$$

where the abbreviation "1st BZ" restricts the variable p_z to the first Brillouin zone. Equation (A9) is the main results of this appendix and can be easily transformed to Eq. (3).

APPENDIX B: HERTZ POTENTIAL AND BASIS FUNCTION

As electromagnetic fields with azimuthal symmetry are easily excited in an MWCNT by a uniform external field, we decided to restrict ourselves to azimuthally symmetric fields. This restriction also holds for finite-length MWCNTs in the long-wavelength regime (Sec. IV B). The electric Hertz vector $\mathbf{\Pi}\equiv\Pi(\rho,z)\mathbf{e}_z$ is then governed by the Helmholtz equation,

$$\frac{1}{\rho}\frac{\partial}{\partial\rho}\left(\rho\frac{\partial\Pi}{\partial\rho}\right)+\frac{\partial^2\Pi}{\partial z^2}+k^2\Pi=0, \tag{B1}$$

where $\mathbf{e}_z$ is the unit vector along the z axis. Since Π depends only on ρ and z, the components of the electric and magnetic fields are as follows:

$$E_\rho=\frac{\partial^2\Pi}{\partial\rho\,\partial z},\quad E_\phi=0,\quad E_z=\left(\frac{\partial^2}{\partial z^2}+k^2\right)\Pi, \tag{B2}$$

$$H_\rho=0,\quad H_\phi=ik\frac{\partial\Pi}{\partial\rho},\quad H_z=0. \tag{B3}$$

With $\kappa=\sqrt{h^2-k^2}$, the basis function $\Phi_p(\rho)$ is taken to satisfy the differential equation

$$\frac{1}{\rho}\frac{d}{d\rho}\left[\rho\frac{d}{d\rho}\Phi_p(\rho)\right]+\kappa^2\Phi_p(\rho)=0,\quad p\in[1,N], \tag{B4}$$

subject to the following boundary conditions at the surface $\rho=R_p$,

$$\frac{\partial}{\partial\rho}\Phi_p(\rho)|_{\rho=R_p+0}-\frac{\partial}{\partial\rho}\Phi_p(\rho)|_{\rho=R_p-0}=\frac{4\pi}{ikc}, \tag{B5}$$

$$\Phi_p(\rho)|_{\rho=R_p+0}=\Phi_p(\rho)|_{\rho=R_p-0}. \tag{B6}$$

The appropriate solution of Eq. (B4) is

$$\Phi_p(\rho)=\frac{4i\pi R_p}{kc}\begin{cases}K_0(\kappa R_p)I_0(\kappa\rho), & \rho<R_p\\ I_0(\kappa R_p)K_0(\kappa\rho), & \rho>R_p,\end{cases} \tag{B7}$$

where $I_0(\cdot)$ and $K_0(\cdot)$ are modified Bessel functions of the zeroth order.

[1] M. S. Dresselhaus, G. Dresselhaus, and Ph. Avouris, *Carbon Nanotubes* (Springer, Berlin, 2001).

[2] S. Reich, C. Thomsen, and J. Maultzsch, *Carbon Nanotubes: Basic Concepts and Physical Properties* (Wiley-VCH, Berlin, 2004).

[3] M. L. Schipper, N. Nakayama-Rachford, C. R. Davis, N. W. S. Kam, P. Chu, Z. Liu, X. Sun, H. Dai, and S. S. Gambhir, Nat. Nanotechnol. **3**, 216 (2008).

[4] G. Ya. Slepyan, S. A. Maksimenko, A. Lakhtakia, O. Yevtushenko, and A. V. Gusakov, Phys. Rev. B **60**, 17136 (1999).

[5] S. A. Maksimenko and G. Ya. Slepyan, in *Electromagnetic Fields in Unconventional Materials and Structures*, edited by O. N. Singh and A. Lakhtakia (Wiley, New York, NY, 2000), pp. 217–255.

[6] S. A. Maksimenko and G. Ya. Slepyan, in *Nanometer Structures: Theory, Modeling, and Simulation*, edited by A. Lakhtakia (SPIE, Bellingham, WA, 2004), pp. 145–206.

[7] M. J. Hagmann, IEEE Trans. Nanotechnol. **4**, 289 (2005).

[8] J. Rybczynski, K. Kempa, A. Herczynski, Y. Wang, M. J. Naughton, Z. F. Ren, Z. P. Huang, D. Cai, and M. Giersig, Appl. Phys. Lett. **90**, 021104 (2007).

[9] A. Raychowdhury and K. Roy, IEEE Trans. Comput.-Aided Des. **25**, 58 (2006).

[10] A. G. Chiariello and G. Miano, Compel **26**, 571 (2007).

[11] A. Maffucci, G. Miano, and F. Villone, Int. J. Circuit Theory Appl. **36**, 31 (2008).

[12] H. Li, W.-Y. Yin, K. Banerjee, and J.-F. Mao, IEEE Trans. Electron Devices **55**, 1328 (2008).

[13] Y. Wang, K. Kempa, B. Kimball, J. B. Carlson, G. Benham, W. Z. Li, T. Kempa, J. Rybczynski, A. Herczynski, and Z. F. Ren, Appl. Phys. Lett. **85**, 2607 (2004).

[14] G. W. Hanson, IEEE Trans. Antennas Propag. **53**, 3426 (2005).

[15] P. J. Burke, S. Li, and Z. Yu, IEEE Trans. Nanotechnol. **5**, 314 (2006).

[16] G. Ya. Slepyan, M. V. Shuba, S. A. Maksimenko, and A. Lakhtakia, Phys. Rev. B **73**, 195416 (2006).
[17] K. Kempa, J. Rybczynski, Z. Huang, K. Gregorczyk, A. Vidan, B. Kimball, J. Carlson, G. Benham, Y. Wang, A. Herczynski, and Z. F. Ren, Adv. Mater. (Weinheim, Ger.) **19**, 421 (2007).
[18] Y. Wang, Q. Wu, W. Shi, X. He, X. Sun, and T. Gui, Int. J. Infrared Millim. Waves **29**, 35 (2008).
[19] G. W. Hanson, IEEE Antennas Propag. Mag. **50**, 66 (2008).
[20] S. A. Maksimenko, G. Ya. Slepyan, A. M. Nemilentsau, and M. V. Shuba, Physica E (Amsterdam) **40**, 2360 (2008).
[21] C. Rutherglen and P. Burke, Nano Lett. **7**, 3296 (2007).
[22] K. Jensen, I. Weldon, H. Garcia, and A. Zettl, Nano Lett. **7**, 3508 (2007); **8**, 374 (2008).
[23] J. A. Misewich, R. Martel, Ph. Avouris, J. C. Tsang, S. Heinze, and J. Tersoff, Science **300**, 783 (2003).
[24] J. Chen, V. Perebeinos, M. Freitag, J. Tsang, Q. Fu, J. Liu, and Ph. Avouris, Science **310**, 1171 (2005).
[25] O. V. Kibis and M. E. Portnoi, Tech. Phys. Lett. **31**, 671 (2005).
[26] O. V. Kibis, M. Rosenau da Costa, and M. E. Portnoi, Nano Lett. **7**, 3414 (2007).
[27] K. G. Batrakov, P. P. Kuzhir, and S. A. Maksimenko, Proc. SPIE **6328**, 63280Z (2006).
[28] P. Kuzhir, K. Batrakov, and S. Maksimenko, Synthesis and Reactivity in Inorganic, Metal-Organic, and Nano-Metal Chemistry **37**, 341 (2007).
[29] K. G. Batrakov, P. P. Kuzhir, and S. A. Maksimenko, Physica E (Amsterdam) **40**, 1065 (2008).
[30] G. Miano and F. Villone, IEEE Trans. Antennas Propag. **54**, 2713 (2006).
[31] J. Hao and G. W. Hanson, Phys. Rev. B **74**, 035119 (2006).
[32] J. Hao and G. W. Hanson, Phys. Rev. B **75**, 165416 (2007).
[33] M. V. Shuba, S. A. Maksimenko, and A. Lakhtakia, Phys. Rev. B **76**, 155407 (2007).
[34] Y. Huang, W.-Y. Yin, and Q. H. Liu, IEEE Trans. Nanotechnol. **7**, 331 (2008).
[35] Y. Lan, B. Zeng, H. Zhang, B. Chen, and Z. Yang, Int. J. Infrared Millim. Waves **27**, 871 (2007).
[36] S. Bandow, M. Takizawa, K. Hirahara, M. Yudasaka, and S. Iijima, Chem. Phys. Lett. **337**, 48 (2001).
[37] S. Iijima, Nature (London) **354**, 56 (1991).
[38] M. Ge and K. Sattler, Science **260**, 515 (1993).
[39] S. Wang and M. Grifoni, Phys. Rev. Lett. **95**, 266802 (2005).
[40] R. Saito, G. Dresselhaus, and M. S. Dresselhaus, J. Appl. Phys. **73**, 494 (1993).
[41] P. Lambin, V. Meunier, and A. Rubio, Phys. Rev. B **62**, 5129 (2000).
[42] K.-H. Ahn, Y.-H. Kim, J. Wiersig, and K. J. Chang, Phys. Rev. Lett. **90**, 026601 (2003).
[43] Y.-G. Yoon, P. Delaney, and S. G. Louie, Phys. Rev. B **66**, 073407 (2002).
[44] A. M. Lunde, K. Flensberg, and A.-P. Jauho, Phys. Rev. B **71**, 125408 (2005).
[45] Y. H. Ho, G. W. Ho, S. C. Chen, J. H. Ho, and M. F. Lin, Phys. Rev. B **76**, 115422 (2007).
[46] Y.-K. Kwon and D. Tomanek, Phys. Rev. B **58**, R16001 (1998).
[47] A. A. Abrikosov, D. V. Livanov, and A. A. Varlamov, Phys. Rev. B **71**, 165423 (2005).
[48] P. N. D'yachkov and D. V. Makaev, Phys. Rev. B **74**, 155442 (2006).
[49] M. A. Tunney and N. R. Cooper, Phys. Rev. B **74**, 075406 (2006).
[50] B. Bourlon, C. Miko, L. Forro, D. C. Glattli, and A. Bachtold, Phys. Rev. Lett. **93**, 176806 (2004).
[51] C. A. Balanis, *Antenna Theory: Analysis and Design* (Wiley, New York, NY, 1997).
[52] A similar situation exists in the theory of skin effect in metals; see L. D. Landau and E. M. Lifshitz, *Electrodynamics of Continuous Media* (Pergamon, Oxford, 1981), Sec. 87; the Leontovich impedance boundary condition does not describe the electromagnetic field inside metal but describes the field well outside the metal. Another analogy is with a thin dielectric film; see L. A. Weinstein, *The Theory of Diffraction and the Factorization Method* (Golem, New York, 1969). Double-side impedance boundary conditions (Weinstein-Sivov boundary condition) describe the electromagnetic field outside the film but not inside.
[53] C. J. Chen, *Introduction to Scanning Tunneling Microscopy* (Oxford University Press, New York, 1993).
[54] L. Novotny and B. Hecht, *Principles of Nano-Optics* (Cambridge University Press, Cambridge, 2006).
[55] V. M. Agranovich and V. L. Ginzburg, *Spatial Dispersion in Crystal Optics and the Theory of Excitons* (Wiley, New York, 1966).
[56] E. M. Lifshits and L. P. Pitaevskii, *Physical Kinetics* (Pergamon, Oxford, 1981).
[57] P. Longe and S. M. Bose, Phys. Rev. B **48**, 18239 (1993).
[58] M. F. Lin and Kenneth W.-K. Shung, Phys. Rev. B **47**, 6617 (1993).
[59] M. F. Lin, D. S. Chuu, and K. W.-K. Shung, Phys. Rev. B **56**, 1430 (1997).
[60] G. Gumbs and G. R. Aizin, Phys. Rev. B **65**, 195407 (2002).
[61] F. L. Shyu and M. F. Lin, Phys. Rev. B **62**, 8508 (2000).
[62] D. J. Mowbray, Z. L. Misković, and F. O. Goodman, Phys. Rev. B **74**, 195435 (2006).
[63] A. Naeemi and J. D. Meindl, IEEE Electron Device Lett. **27**, 338 (2006).
[64] W. Wang, S. Haruehanroengra, L. Shang, and M. Liu, Micro Nano Lett. **2**, 35 (2007).
[65] H. J. Li, W. G. Lu, J. J. Li, X. D. Bai, and C. Z. Gu, Phys. Rev. Lett. **95**, 086601 (2005).
[66] A. S. Ilyinsky, G. Ya. Slepyan, and A. Ya. Slepyan, *Propagation, Scattering and Dissipation of Electromagnetic Waves* (Peter Peregrinus, London, 1993).
[67] D. Colton and R. Kress, *Integral Equation Methods in Scattering Theory* (Wiley, New York, NY, 1983).
[68] E. Wolf, Astrophys. Space Sci. **227**, 277 (1995).
[69] M. Born and E. Wolf, *Principles of Optics* (Pergamon, Oxford, 1999).
[70] R. W. P. King and T. T. Wu, IEEE Trans. Antennas Propag. **14**, 524 (1966).
[71] S. A. Maksimenko, A. A. Khrushchinsky, G. Ya. Slepyan, and O. V. Kibis, J. Nanophotonics **1**, 013505 (2007).
[72] C.-K. Lee, J. Cho, J. Ihm, and K.-H. Ahn, Phys. Rev. B **69**, 205403 (2004).
[73] J. M. Pitarke, V. M. Silkin, E. V. Chulkov, and P. M. Echenique, Rep. Prog. Phys. **70**, 1 (2007).
[74] L. Novotny, Phys. Rev. Lett. **98**, 266802 (2007).
[75] A. L. Elias, J. A. Rodriguez-Manzo, M. R. McCartney, D. Golberg, A. Zamudio, S. E. Baltazar, F. Lopez-Urias, E. Munoz-Sandoval, L. Gu, C. C. Tang, D. J. Smith, Y. Bando, H. Terrones, and M. Terrones, Nano Lett. **5**, 467 (2005).

[76] G. W. Hanson, IEEE Trans. Antennas Propag. **54**, 76 (2006).
[77] P. B. Johnson and R. W. Christy, Phys. Rev. B **6**, 4370 (1972).
[78] B. Wang, S. Yin, G. Wang, A. Buldum, and J. Zhao, Phys. Rev. Lett. **86**, 2046 (2001).
[79] K. C. Chin, A. Gohel, W. Z. Chen, H. I. Elim, W. Ji, G. L. Chong, C. H. Sow, and A. T. S. Wee, Chem. Phys. Lett. **409**, 85 (2005).
[80] *Selected Papers on Linear Optical Composite Materials*, edited by A. Lakhtakia (SPIE, Bellingham, WA, 1996).
[81] A 1D analog of state (A3) is the eigenfunction of the system of two identical potential wells separated by a potential barrier; see L. D. Landau and E. M. Lifshitz, *Quantum Mechanics* (Pergamon, Oxford, 1981), Sec. 50, Task 3. The derivation of Eqs. (A3) and (A4) is similar to the solution of that task.